Microstrip resonators
for circuit quantum electrodynamics

Master Thesis

Marta Krawczyk

Supervisor: Prof. Dr. Rudolf Gross

Advisor: Alexander Theodor Baust

December 2011

TECHNISCHE UNIVERSITÄT MÜNCHEN

Contents

Chapter 1

Introduction

The interaction of light and matter is one of the fundamental physical concepts which has been studied thoroughly in the 20th century. Already in 1905, Albert Einstein postulated the existence of quanta of light, that can be absorbed by matter [1]. For his finding he was granted the Nobel prize in 1921. Many interesting experiments have been conducted to reveal the basic physics of light-matter interaction. In the field of cavity quantum electrodynamics (cavity QED) atoms are coupled to light confined between two optical mirrors [2–4]. However, the coupling strength achievable between atoms and photons in the optical regime is very small.

The advent of circuit quantum electrodynamics (circuit QED) allowed for an enhancement of the coupling strengths [5–7]. This is realized by replacing the natural atom by a superconducting two-level system, called qubit, and the optical cavity by an on-chip microwave transmission line resonator. Many concepts established in the optical regime could be retrieved in the microwave regime [8,9]. In addition circuit QED systems can be used for quantum information processing [10, 11].

In order not to be limited by the leakage of photons out of the resonator reasonably large quality factors are required [12]. So far, the resonator systems most commonly used are based on coplanar waveguides (CPW). The CPW resonators exhibit very high quality factors [13–15]. However those structures become inefficient, when the complexity of the involved circuits increases. Specifically, integration of antennas as control structures requires to break the ground plane of the CPW, which results in spurious resonances interfering with the resonator modes.

As a result, the interest in a new resonator type for experiments in circuit QED is increasing. A promising proposal is the microstrip resonator. It is a planar transmission line resonator with the conductor on the top and the ground plane on the bottom of the chip. This geometry is very convenient, since other structures like qubits and antennas can be placed on the top of the substrate in close vicinity of the conductor.

Additionally, the microstrip resonators are well known for having background spectra without parasitic modes.

There are, however, two basic challenges in the application of microstrip in the field of circuit QED. The quality factors of microstrip resonators have not been studied extensively yet. Additionally, we have to consider how to realize coupling of qubits to microstrip resonators.

The aim of this thesis is to investigate whether microstrip resonators can be successfully applied in circuit QED. If the microstrip-based technology should compete with CPW technology we have to have full control of the parameters of our circuits. Not only we have to be able to maximize the quality factors of the resonators. We also need to extend the knowledge of parasitic modes in the microstrip spectra. In addition we have to assure that the control structures required for circuit QED will not deteriorate the performance of the circuits.

This task requires a systematic procedure including all important elements of the analysis. The numerous different details of the microstrip geometry have to be taken into consideration. Different techniques of the production process have to be mastered reliably. Since the structures have to be characterized at cryogenic temperatures, a measurement set-up with a large throughput is required. The last important aspect to mention is that a theoretical toolbox to predict and describe the behavior of the circuits is needed.

This thesis is structured as follows. In the second chapter we present the theoretical background for understanding of microstrip resonators. We also explain the basics of the measurement technique. In Chapter 3 we discuss in details crucial elements of the design, production and measurement process. In Chapter 4 the results of our measurements are shown and analyzed. A qualitative and quantitative evaluation of our data is contained in Chapter 5.

Chapter 2

Theory

In this thesis we study electrical circuits called microstrip resonators. An electrical resonator is a system characterized by a resonant frequency ω_0. This frequency gives a rate of periodic exchange of electric and magnetic energy in the system.

The resonator types, most commonly used for experiments in circuit QED presently, are coplanar waveguide (CPW) resonators (cf. Section 2.1). However, in this thesis we study the microstrip resonators which have numerous advantages over the CPW structures. The considered resonators consist of microstrip transmission lines which are structures transmitting electromagnetic waves (cf. Section 2.2).

There are many methods to describe the behavior of microstrip resonant circuits [16–18]. Here we apply the lumped element LRC model which describes the behavior of a microwave resonator near its resonant frequency very well. A detailed description will be presented in Section 2.3.

A very important parameter of a resonator is its quality factor Q. The definition is given by [19]

$$Q = \frac{\omega \,(\text{average energy stored in the resonator})}{\text{energy loss per second}}, \tag{2.1}$$

where ω is the frequency. Therefore the quality factor is a measure of the circuit's losses. There are several loss mechanisms in a microstrip resonator, which we will describe in Section 2.4. In Section 2.5 we discuss the theoretical foundation of the measurement technique.

2.1 The microwave resonators for circuit QED

The relevant energy scale of circuit QED experiments is in the microwave regime $(1 - 100 \text{ GHz})$. Therefore suitable cavities in the microwave regime are required. An
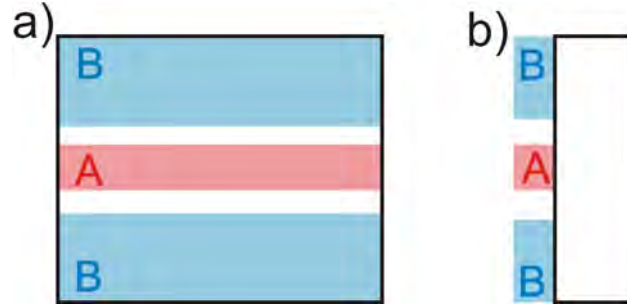
Figure 2.1: Scheme of a coplanar waveguide. Colored rectangles represent conducting structures and the white rectangle pictures the dielectric layer. Drawings are not to scale. a) Top view. The conducting strip (A) is placed on the top of the dielectric layer between two conducting ground planes (B). b) Side view.

important type of a transmission line resonator is the coplanar waveguide (CPW) resonator. It is based on CPW transmission lines which are presented in Fig. 2.1. A conventional coplanar waveguide consists of a center strip conductor with semi-infinite ground planes on either side.

Presently CPW-based resonators are the most commonly used resonators in the field of circuit quantum electrodynamics [12, 13]. Therefore, their characteristics which are relevant for circuit QED have been studied thoroughly in many aspects. The power and temperature dependence of their quality factors have been examined in details [20]. In order to investigate the loss mechanisms of CPW resonators the influence of different substrate and conductor materials on the behavior of the resonators have been examined [21]. In addition the influence of different types of geometris have been studied [22]. Furthermore the coupling mechanisms of CPW have been investigated as well [13, 23].

Contrary to CPW resonators, the microstrip-based technology is well established in engineering to convey signals in microwave regime. This is mainly due to the compact structure of microstrip resonant circuits. However, the application of microstrip resonators in circuit QED has not been investigated yet to our knowledge. This is due to the lower quality factors and higher radiation losses of microstrip resonators. Nevertheless, the microstrip resonators have many advantages compared to CPW resonators. One important aspect is the spectrum of microstrip resonators well known for containing nearly no parasitic modes. In addition, the geometry of microstrip allows for the straightforward implementation of additional circuit elements and control lines in cloes wicinity to the resonator. Therefore, the major aim of this thesis is to examine microstrip resonant circuits as cavities for application in circuit QED.
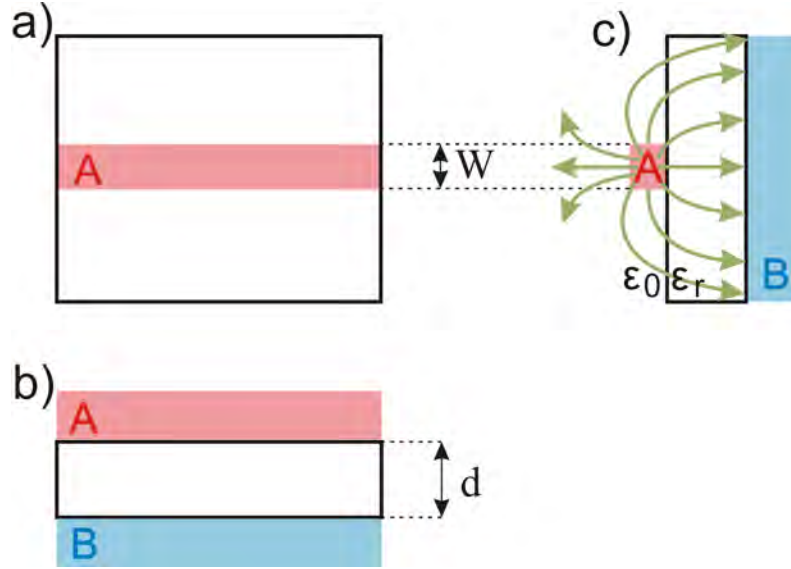
Figure 2.1: Scheme of a microstrip transmission line. Colored rectangles represent conducting structures and the white rectangle pictures the dielectric layer. Drawings are not to scale. a) Top view. The conducting strip (A) is placed on the top of the dielectric layer. b) Side view. A conducting ground plane (B) resides on the bottom of the chip. c) Cross section through the microstrip. Arrows represent the electric field lines, which spread in the surrounding medium (vacuum permittivity ε_0 assumed here) as well as in the dielectric layer (relative permittivity ε_r) [24].

2.2 The microstrip transmission line

Transmission lines are structures specialized on transmitting electromagnetic waves at radio frequencies i.e. between $300\,\text{kHz}$ and $300\,\text{GHz}$ [25]. There are many types of transmission lines with different geometries and characteristics [26]. Each type has its advantages and disadvantages depending on the respective application. In the present thesis we use transmission lines of the microstrip type. Microstrips are planar transmission lines consisting of a conducting strip and a ground plane separated by a dielectric (cf. Fig. 2.1).

In a transmission line the inductance L, capacitance C, resistance R and conductance G are uniformly distributed along the length of the line [24]. It is convenient to model small segments of a transmission line in terms of lumped elements as presented in Fig. 2.2. We can understand the elements of the model as a representation of physical phenomena occurring in the transmission line. The lower line (Signal "-") in Fig. 2.2b represents the niobium ground plane on the bottom of the substrate and the upper line (Signal "+") is the conducting strip on the top (cf. Fig. 2.3). The inductance per unit length L' describes the inductance associated with the ground plane and the conductor. The capacitance per unit length C' originates from the immediate vicinity
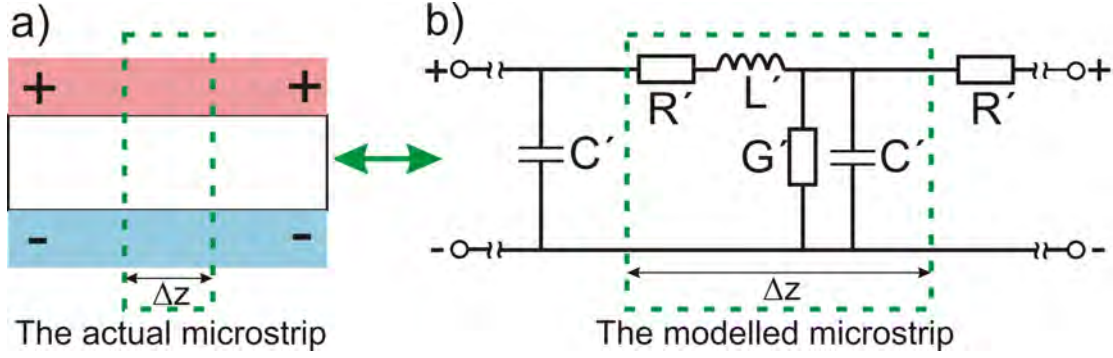
Figure 2.2: Lumped-element representation of an infinitesimal part Δz of a microstrip transmission line. a) The total transmission line is a series connection of circuits of length Δz. b) Model of a small segment of the transmission line of the length Δz. The elements L', C', L' and G' are per unit length of the transmission line.

of the conducting layers. The resistance per unit length R' is the resistance of the conductors. The shunting conductance per unit length G' describes the losses in the dielectric layer.

Ttransmission lines applied in practical applications exhibit low loss [27]. Using the Telegrapher's equations [24] one calculates the wavelength λ of the signals propagating along the transmission line,

$$\lambda = \frac{2\pi}{\omega\sqrt{L'C'}}. \tag{2.1}$$

The phase velocity v_{ph} is given by the formula [24]

$$v_{\mathrm{ph}} = \frac{1}{\sqrt{L'C'}}. \tag{2.2}$$

Two important quantities defining a transmission line are the characteristic impedance Z_0 [24]

$$Z_0 = \sqrt{\frac{L'}{C'}}, \tag{2.3}$$

and the propagation constant β

$$\beta = k_0\sqrt{\varepsilon_{\mathrm{eff}}}, \tag{2.4}$$

where k_0 is the propagation constant of the surounding medium and $\varepsilon_{\mathrm{eff}}$ is the effective permittivity of the surrounding medium.

As it is presented in Fig. 2.1c the electric field lines of the microstrip exist in the dielectric layer as well as in the surrounding medium (here the latter is assumed to be air). As a result, the effective permittivity ε_{eff} is between the dielectric constant of the

surrounding medium ($\varepsilon_{eff} = 1$) and the dielectric constant of the substrate ε_r. For our microstrip ε_{eff} is given approximately by [24]

$$\varepsilon_{\text{eff}} \approx \frac{\varepsilon_{\text{r}} + 1}{2} + \frac{\varepsilon_{\text{r}} - 1}{2} + \frac{1}{\sqrt{1 + 12d/W}}, \tag{2.5}$$

where d is the thickness of the dielectric substrate and W is the width of the of conducting strip (cf. Fig. 2.1). The characteristic impedance Z_0 of a microstrip line is determined by its geometry and by the effective dielectric constant ϵ_{eff} [24]:

$$Z_0 \approx \begin{cases} \frac{60}{\sqrt{\varepsilon_{\text{eff}}}} \ln\left(\frac{8d}{W} + \frac{W}{4d}\right) & \text{for } W/d \leq 1, \\ \frac{120\pi}{\sqrt{\varepsilon_{\text{eff}}}[W/d + 1.393 + 0.667 \ln(W/d + 1.444)]} & \text{for } W/d \geq 1. \end{cases} \tag{2.6}$$

2.3 The microstrip resonator

2.3.1 The uncoupled resonator

Transmission lines discussed in the previous section have the very important property that voltage and current vary significantly in magnitude and phase over their length. In Fig. 2.1 we show the current and voltage distribution in a transmission line which is open circuited at both ends [28]. Such a transmission line acts as a resonator whose length is equal to the half of the wavelength of its ground mode [24]. Therefore it is called a $\lambda/2$ resonator.

It is a convenient and common [12, 13, 19, 24, 29] practice to model a $\lambda/2$ resonator in the vicinity of the resonant frequency as a parallel connection of a resistor R, an inductor L and a capacitor C as presented in Fig. 2.2. The description of this so called "lumped element model of a transmission line resonant circuit" is mainly based on the book by David M. Pozar [24] and the article of Martin Göppl $et.al.$ [13]. The input impedance Z_{in} of this circuit is given by

$$Z_{\text{in}} = \left(\frac{1}{R} + \frac{1}{i\omega L} + i\omega C\right)^{-1}, \tag{2.1}$$

where ω is the frequency and i is the imaginary unit. The complex input power P_{in} at the resonator's input is given by [19]

$$P_{\text{in}} = \frac{1}{2}|V|^2 \left(\frac{1}{R} + \frac{1}{i\omega L} + i\omega C\right)^{-1}, \tag{2.2}$$

where V is voltage. The $\frac{1}{R}$-term in this equation represents the energy W_{loss} dissipated in the resistor. The complex terms represent the magnetic energy W_m stored in the inductor and the electric energy W_e stored in the capacitor, respectively. Resonance
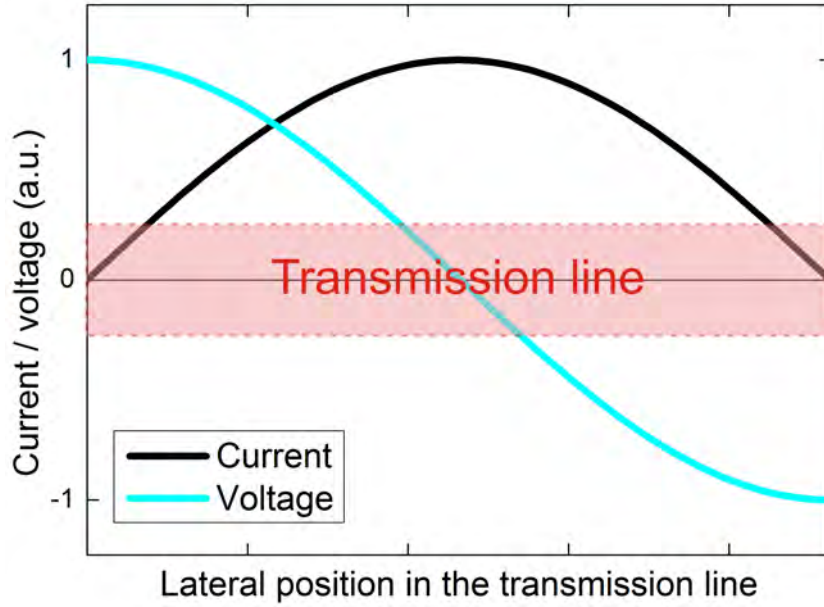
Figure 2.1: Current and voltage distribution in an open circuited transmission line [24]. Such a transmission line behaves like a resonator which is not coupled to external circuitry. Due to the fact that the length of the resonator is equal to the half of the wavelength of its ground mode it is called a $\lambda/2$-resonator.

Figure 2.2: Lumped element model of a microstrip resonant circuit. In the vicinity of the resonant frequency the resonator is modeled as a resistor R, an inductor L and a capacitor C.

occurs when the resonator is able to convert the magnetic energy to the electric energy. To fulfill this condition $W_e = W_m$ must hold. Therefore the unloaded resonant frequency ω_0 is given by

$$\omega_0 = \frac{1}{\sqrt{LC}}. \tag{2.3}$$

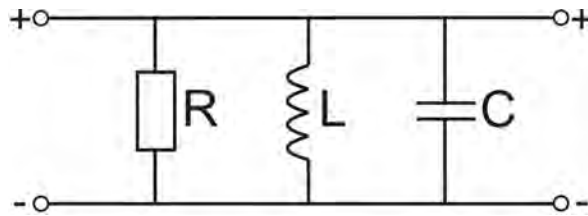This is the frequency of the fundamental mode of the resonator. The resonant frequency of the nth mode of the resonator is given by

$$\omega_n = n\omega_0 = \frac{1}{\sqrt{L_{\text{n}}C}}, \tag{2.4}$$

where [13]

$$L_{\text{n}} = Ln^2 \tag{2.5}$$

and $n \geq 1$ is an integer number. Then the internal quality factor of the resonant circuit is given according to Equation 2.1 by

$$Q_{\text{int}} = \omega_{\text{n}} \frac{2W_{\text{m}}}{W_{\text{loss}}} = \frac{R}{\omega_{\text{n}} L_{\text{n}}} = \omega_{\text{n}} RC. \tag{2.6}$$

2.3.2 The coupled resonator

If we now want to characterize a resonant circuit we have to couple it to external circuitry. In our case this is done via gap coupling. A scheme of the considered geometry is presented in Fig. 2.3. The circuit consists of two building blocks, the $\lambda/2$ resonator and the feed lines. Both of them are transmission lines of the microstrip type (cf. Section 2.2). The main concept of the resonator is to store energy. Feed lines serve solely to couple external circuits to the resonator. Another important element of the circuit is the gap between the feed lines and the resonator. The effect of the gap is represented by a coupling capacitance C_{k} (cf. Fig. 2.4a). A resistor R_{L} models the feed line.

For further analysis the series connection of the coupling capacitance C_{k} and the resistor R_{L} is replaced by its Norton equivalent circuit[1]. The Norton equivalent circuit consists of a resistor R^* and a capacitor C^* (cf. Fig. 2.4b) with

$$R^* = \frac{1 + \omega_{\text{n}}^2 C_{\text{k}}^2 R_{\text{L}}^2}{\omega_{\text{n}}^2 C_{\text{k}}^2 R_{\text{L}}} \tag{2.7}$$

---

[1]Norton's theorem states that any collection of voltage sources V, current sources I, and resistors R with two terminals is equivalent to a parallel connection of an ideal current source I^* and a single impedance R^* [30]. The theorem is valid for direct current systems as well as for alternating current systems.
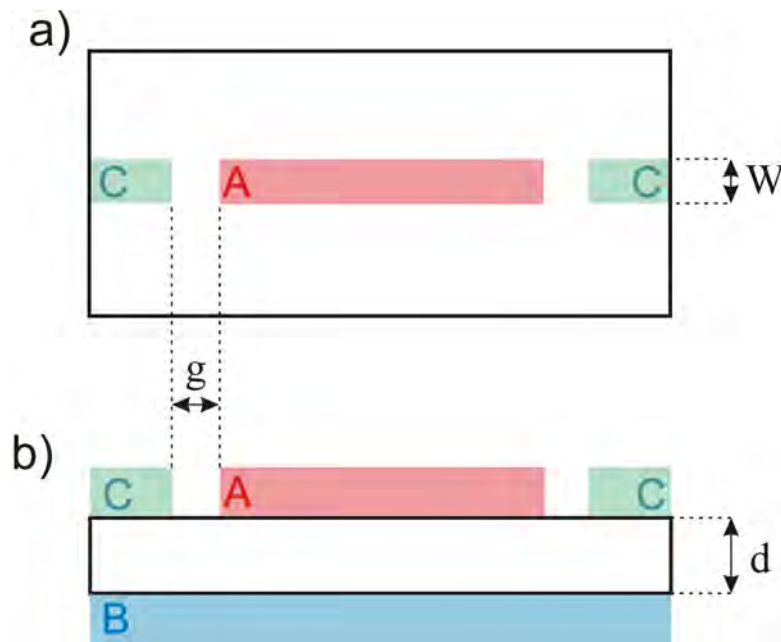
Figure 2.3: Scheme of a resonant circuit made of microstrips. Colored rectangles represent conducting structures and the white rectangle pictures the dielectric layer. Drawings are not to scale. a) Top view. Coupling of the resonator (A) to the feed lines (C) is realized by a gap of width g. b) Side view. A conducting ground plane (B) resides on the bottom of the chip .

Figure 2.4: Lumped element model of a coupled resonant circuit. Blue areas contain the model of the resonator (cf. Fig. 2.2). a) The gap is modeled as a coupling capacitance C_k. The input and output circuitry (gray areas) are modeled by a load resistor R_L. b) The elements R^* and C^* are Norton equivalents of C_k and R_L [30].

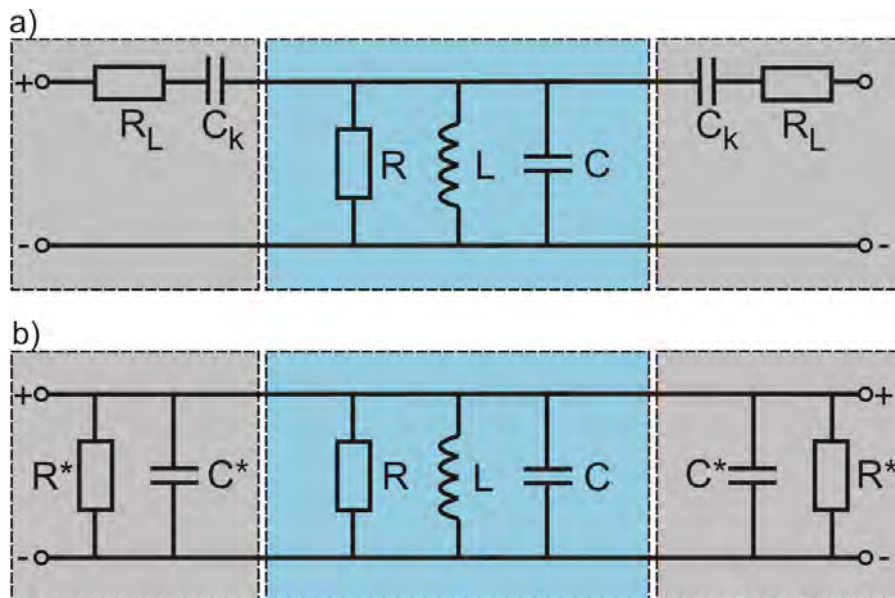and

$$C^* = \frac{C_k}{1 + \omega_n^2 C_k^2 R_L^2}. \tag{2.8}$$

Then the loaded the quality factor Q_L is reduced due to the resistive loading, yielding

$$Q_L = \omega_n^* \frac{C + 2C^*}{1/R + 2/R^*} \tag{2.9}$$

with the loaded resonant frequency ω_n^*. The latter takes into account the effect of capacitive loading and is given by

$$\omega_n^* = \frac{1}{\sqrt{L_n \left(C + 2C^* \right)}}. \tag{2.10}$$

The external quality factor Q_{ext} is given by

$$Q_{ext} = \frac{\omega_n R^* C}{2}. \tag{2.11}$$

To conclude the discussion, the internal quality factor Q_{int} represents the losses in the resonator (compare Subsection 2.4.1). The external quality factor Q_{ext} is influenced by the losses in the gap and in the feedlines (cf. Subsection 2.4.2). The loaded quality factor Q_L is a parallel combination of the internal quality factor Q_{int} and the external quality factor Q_{ext},

$$\frac{1}{Q_L} = \frac{1}{Q_{int}} + \frac{1}{Q_{ext}}. \tag{2.12}$$

2.4 Losses in the microstrip resonator

2.4.1 The uncoupled resonator

There are three major loss mechanisms in the microstrip resonator. These are of the *resistive*, *dielectric*, and *radiative* origin [31]. We first consider the *resistive* mechanism.

We use niobium for the conducting layer. Niobium is a superconductor of type II. Below the critical temperature T_C the superconductor is in the superconducting state. The two-fluid model describes the behavior of superconductors at temperatures $T < T_C$ [27]. It explains the behavior of the superconducting transmission lines in an alternating field well (cf. Fig. 2.1). The model postulates the existence of two types of charge carriers, the normal electrons and the superelectrons. The normal electrons are associated with the unpaired electrons and the superelectrons represent Cooper pairs [32]. Both types of charge carriers contribute to the current. The density of
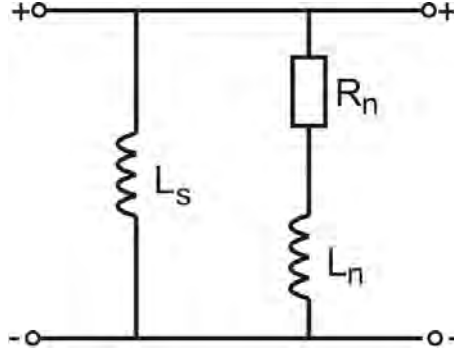
Figure 2.1: Lumped element representation of a superconductor with the superconducting channel and the normal conducting channel. The inductor L_s represent the inductance associated with the Cooper pairs. The resistor R_n and the inductor L_n accounts for the influence of the unpaired electrons.

superelectrons n_s is related to the density of the normal electrons n_n as [27]

$$n_s = \frac{1}{2} n_n \left(1 - \left(\frac{T}{T_C} \right)^4 \right), \qquad T < T_C. \tag{2.1}$$

Therefore the density of Cooper pairs increases when the temperature decreases. The factor $\frac{1}{2}$ in Equation (2.1) can be understood considering that the density of unpaired electrons is twice the density of Cooper pairs. At $T = 0$ the density of the normal electrons would be zero because all unpaired electrons would be coupled to Cooper pairs.

Let let us again consider the "lumped element representation" (cf. Subsection 2.3.1). The resistor R_n and inductor L_n (compare Fig. 2.1) describe the behavior of normal electrons. The superconducting channel is represented by the inductor L_s. If one applies a direct current ($\omega = 0$) to the circuit, then the impedance $Z_s = i\omega L_s$ behaves like a short circuit and no current flows through the normal channel. So the resistance of our circuit vanishes. However, if we apply an alternating current with frequency $\omega \neq 0$, part of the current will flow through the normal channel and we have to take the resistance into consideration. For niobium ($T_C = 9.2\,\mathrm{K}$ [33]) at frequency $1.3\,\mathrm{GHz}$ and temperature $4.2\,\mathrm{K}$ the resistance R_n is about $800\,\mathrm{n\Omega}$ [34].

Now let us turn to the *dielectric losses*. They are mainly caused by unsaturated two level systems (TLS) [35]. Those are defects in the substrate which absorb energy. At high temperature and high energy TLS are saturated and do not contribute to the dielectric loss [20]. The dissipation due to the unsaturated TLS at low temperature and low power is of a relatively large magnitude and can dominate other effects [36].

Finally, we consider the *radiation losses*. The size of our circuit is of the order of magnitude of the wavelength of the applied signals (compare Fig. 2.1). Therefore the

resonator will behave as an antenna radiating some of its energy into the environment [37].

Let us summarize the effect of the above described phenomena. We introduce attenuation constants α_c for the *resistive losses* in the conductor, α_d for the *dielectric losses* and α_r for the *radiation losses*. The total attenuation α of the microstrip line is given by

$$\alpha = \alpha_c + \alpha_d + \alpha_r. \tag{2.2}$$

The internal quality factor of the resonator takes all the described loss mechanisms into consideration is given by [13]

$$Q_{\text{int}} = \frac{\pi}{2\alpha l}, \tag{2.3}$$

where l is the length of the resonator.

2.4.2 The coupled resonator

Let us now consider a resonator that is gap-coupled to the feed lines as presented in Fig. 2.3. Due to this coupling to the environment energy is partially transmitted from the resonator into the feed lines [31]. These losses are represented by the external quality factor Q_{ext} which is determined by the coupling capacitance (cf. Subsection 2.3.2).

Depending on the value of the coupling capacitance the resonators are divided into two classes [24]. If the coupling capacitance is small, then the resonator is called *undercoupled*. In the extreme case of an uncoupled resonator ($C = 0$) the loaded quality factor Q_L is governed by the intrinsic losses in the resonator (cf. Subsection 2.4.1). For the uncoupled resonator it is possible to investigate the internal quality factor Q_{int} [29]. If the coupling capacitance is large, then the resonator is called *overcoupled*.

2.5 The measurement technique

The fundamental problem one faces when analyzing transmission lines is to measure voltages and currents directly, because they vary significantly along the length of the transmission line (cf. Fig. 2.1). Therefore, the wave quantities are taken into consideration [38]. Let us consider a 2-port network like the one presented in Fig. 2.1. We first apply the incident wave V_1^+ at the first port, while the second port is terminated with a matched impedance. In this way no signal is reflected at the second port and we have $V_2^+ = 0$. The transmission parameter S_{21} is defined as the ratio of the voltage of the transmitted wave V_2^- to the incident wave V_1^+. The reflection parameter S_{11} is
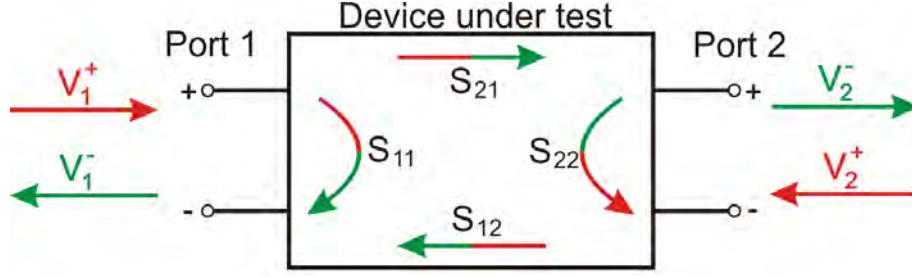
Figure 2.1: A model of a 2-port network with the scattering parameters. The figure was adopted from [38].

the ratio of the reflected wave V_1^- to the incident wave V_1^+. The scattering parameters S_{12} and S_{22} are determined by measuring in the opposite direction, when the first port is terminated with a matched impedance. We summarize the scattering parameters in the scattering matrix $\mathbf{S}$ [24] as follows

$$\begin{bmatrix} V_1^- \\ V_2^- \end{bmatrix} = \begin{bmatrix} S_{11} & S_{12} \\ S_{21} & S_{22} \end{bmatrix} \begin{bmatrix} V_1^+ \\ V_2^+ \end{bmatrix} \tag{2.1}$$

or

$$\mathbf{V}^- = \mathbf{S}\mathbf{V}^+. \tag{2.2}$$

Chapter 3

Experimental technique

During the work on this thesis 43 resonators were designed, produced and measured. In this chapter we discuss the procedure and tools required to develop, fabricate and measure the samples.

First we designed the basic microstrip structure (compare Section 3.1). It consisted of a microstrip resonator, two feed lines and a ground plane. Empirical data [39] as well as calculated quantities determined the final design of the structures. Then we introduced additional features such as antennas and constrictions. The purpose was to examine the application of microstrip resonators in the field of circuit quantum electrodynamics.

We have coated the silicon substrates with niobium by means of the sputter deposition technique (Section 3.2). The films were then patterned using optical lithography. The frequency dependent transmission properties of the produced samples were then measured as we will present in (Section 3.3).

3.1 The design process

3.1.1 Microstrips without constrictions and antennas

The resonant circuits analyzed in this thesis are microstrip resonators, which are thin film structures patterned in a niobium layer (compare Fig. 3.1). They are symmetric with respect to the center point of the chip and consist of two feed lines and a resonator. The structures are distributed element circuits and their physical behavior is described by transmission line theory (cf. Chapter 2.2). We note the fact that physical characteristics of a microstrip resonator are influenced by its geometrical parameters. In Table 3.1 we show which quantity is affected by which parameter.

Now let us discuss how some of those parameters were designed. In Fig. 3.1 we show
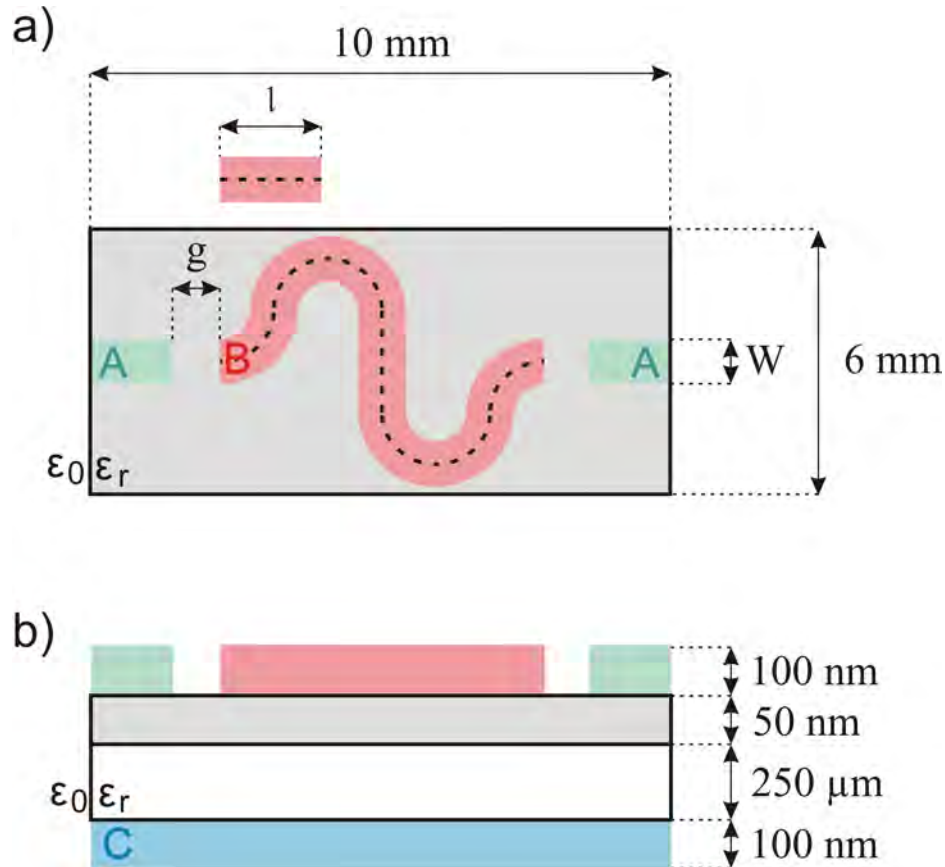
Figure 3.1: Design scheme of a microstrip resonant circuit. Colored rectangles represent niobium structures. The white rectangle is the silicon substrate (dielectric permittivity $\varepsilon_r = 11.9$ [40]) with 50 nm thermal silicon oxide on top (gray region). Drawings are not to scale. a) Top view. The gap width g defines the coupling capacitance between the resonator transmission line (B) and the feedlines (A). The transmission line is bent to fit onto the substrate. The length of the resonator is the length of the black dashed line. b) Side view. On the bottom of the chip there is a ground plane (C) made of niobium. The thicknesses of the niobium film $t = 100$ nm was kept constant for all samples.

Geometrical parameter	Quantity it influences
g	Coupling capacitance, resonant frequency, external quality factor
l	Resonant frequency, internal quality factor
W	Characteristic impedance of the line, internal quality factor, resonant frequency
t	Characteristic impedance of the line, resonant frequency
d	Characteristic impedance of the line
ε_r	Characteristic impedance of the line, internal quality factor

Table 3.1: The geometry of the microstrip resonator influences its characteristics. This table presents the possibilities to vary the performance of a resonant circuit by changing its parameters: gap width (g), length of the resonator (l), width of the transmission line (W), thickness of the transmission line (t), thickness of the substrate (d), type of the substrate (ε_r). (compare Chapter 2.2).

a scheme of a microstrip resonator. Feed lines are designed to realize coupling between the resonator line and external circuitry. Since we wanted to examine the influence of the coupling capacitance, we varied the gap width for the first sample series.

The length of the resonator l determines the value of the resonant frequency f_0 according to

$$l = \frac{c}{2 f_0 \sqrt{\varepsilon_\mathrm{eff}}}. \qquad (3.1)$$

Our aim was to keep the resonant frequency constant at $5.75\,\mathrm{GHz}$. The reason is the Dual-Path method which was developed at the WMI and is used for characterizing circuit QED systems [41]. A key element of this method is a hybrid ring, which is optimized for the above mentioned frequency [42]. Since the required length of the resonator was larger then the size of the chip, the line was bent, so that it could fit onto the chip. This inevitably introduced additional capacitances and inductances into the circuit [43]. Thus Equation (3.1) could give us only an approximate value of the required resonator length. In order to determine the exact value l_emp we collected the data on previously examined microstrip structures [39]. We compared their lengths l_prev with the measured resonant frequencies $f_\mathrm{0,prev}$ and thus obtained the required relation for the exact length of the resonator l_emp:

$$l_\mathrm{emp} = \frac{l_\mathrm{prev}\, f_\mathrm{0,prev}}{f_0}. \qquad (3.2)$$
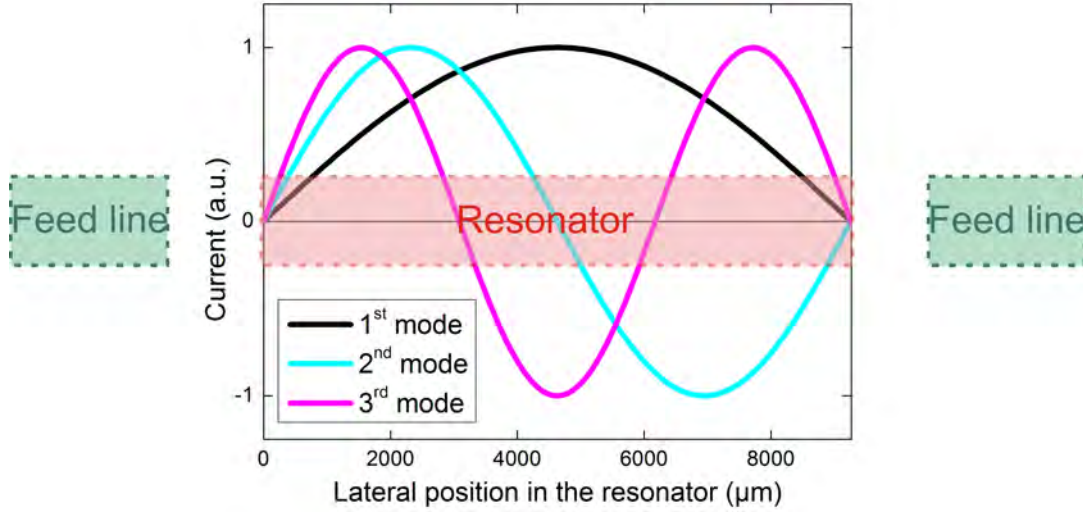
Figure 3.2: Current distribution for the first, second and third harmonic mode in an open-circuited microstrip resonator ($\lambda/2$ resonator) [24]. In the middle of the resonator the current of the fundamental mode has its maximum. By inserting an antenna at different positions of the circuit we checked how the performance of the circuit changed.

3.1.2   Microstrip with constrictions and antennas

Apart from characterizing the basic microstrip structures we also proved their usability for experiments in the field of circuit quantum electrodynamics [29]. One major aspect of this field of physics deals with the coupling phenomenon of quantum bits (qubits) to transmission line resonators. Interaction in the ultrastrong regime was achieved by coupling qubits to a CPW resonator galvanically [12]. Galvanic coupling is realized when a qubit and a resonator share a part of the transmission line. Since the dimensions of the qubit (order of µm [12]) are much smaller than those of the microstrip resonator (our resonators are 200 µm wide) the microstrip has to be constricted to enable galvanic coupling. A change of the width of the resonator induces a change in its characteristic impedance, which introduces disturbances to the circuit [24]. Thus for galvanic coupling of microstrips to qubits the effect of constrictions on the performance of microstrip resonant circuits has to be examined.

For this purpose we have designed microstrip resonators with constrictions of length 80 µm. The constriction interacts with different modes of the current depending on its position in the resonator (Fig. 3.2). We placed our constrictions in the middle of the microstrip. We have designed structures with different widths of constrictions. The narrowest structure produced was 2 µm wide, which was close to the resolution limit of optical lithography (1 µm) [44]. We have designed a smooth transition, like it is presented in Fig. 3.3 to avoid additional disturbances introduced to the circuit. Our
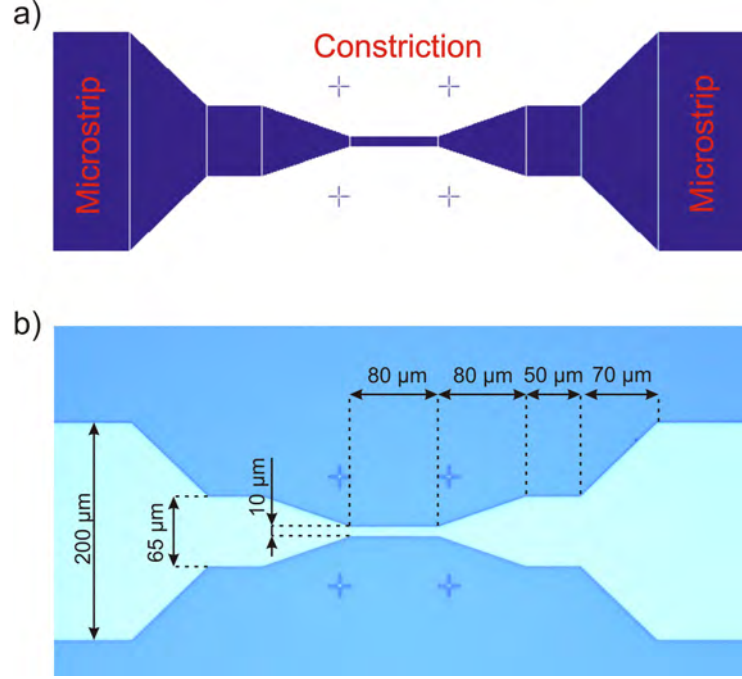
Figure 3.3: A microstrip resonator with constriction of width $10\,\mu$m and length $80\,\mu$m. a) Dark blue region is the designed structure. The four alignment marks in the middle area were designed for purpose of electron beam lithography, which is used to write qubits [45]. b) An optical microscope image of a constricted microstrip. The lighter regions are niobium structures. The transition from the thick line ($Z_0 = 50\,\Omega$) to the thin line ($Z_1 = 120\,\Omega$) is made gradually as recommended by [29].

structure is based on the design presented in [12, 29].

A second important structure for experiments with qubits is an antenna. It is used for microwave irradiation of flux qubits to induce transitions from the ground to the excited state. This enables time-domain measurements and qubit spectroscopy [29]. We designed a $50\,\Omega$ impedance matched CPW transmission line which is short-circuited at the end and thus acts as an antenna (Fig. 3.4). It consists of a $20\,\mu$m wide niobium inner conductor with a pair of niobium ground planes on both sides. The conductors near the chip boundaries are wider to enable connection with the pins of SMA connectors. We placed antennas in the vicinity of the microstrip line at different positions of the resonator. The intention was to examine how the antennas interact with different modes of the electric field of the resonator (compare Fig. 3.2). An overview of the designed structures can be found in Appendix C.
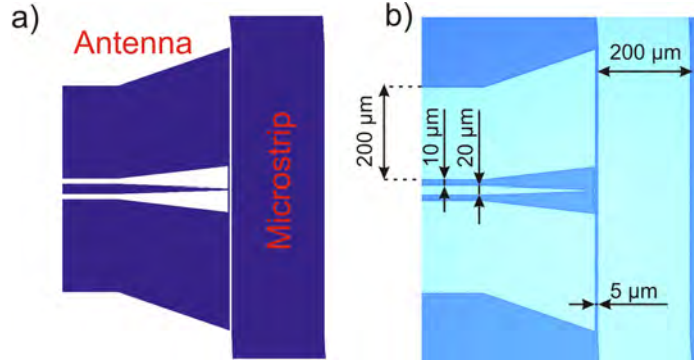
Figure 3.4: A microstrip resonator with an antenna. The position of the antennas was varied to examine how the behavior of our resonator changes (cf. Fig. 3.2) a) LayoutEditor view of the designed structure. b) An optical microscope image of the produced structure.

3.2   The fabrication process

After cleaning the silicon substrate (Fig. 3.1a) we sputtered a niobium film onto both sides of the substrate (Fig. 3.1b). Sputtering was done by creating ions of niobium and then accelerating them onto the silicon substrate in a dc-magnetron chamber.

Then the niobium films were patterned by means of the optical lithography technique[1]. This technique applies the characteristics of a positive photoresist [46], which is a polymer) that becomes soluble in a photoresist developer after being exposed to UV light. We used an optical mask made of fused quartz transparent for UV radiation. The quartz substrate was covered with the desired structure made of an UV absorbing film.

The details of the process are depicted in Fig. 3.1. The resist AZ 5214 was spin coated on the chip (3.1c). Then the sample was soft-baked at $110\,^{\circ}$C to remove residues of the solvent from the photoresist layer. The sample was then covered with the optical mask and radiated with UV light (3.1d). In this manner only the regions not covered with the chromium structures were exposed. Subsequently the sample was put in AZ 726 MIF developer. In this way we patterned the desired structure in the photoresist film. Afterwards the sample was reactive ion etched (RIE). During this process the niobium film not covered by the photoresist was etched using a physical process with argon ions and a chemical process with SF_6 [47]. After removal of polymer residues in a hot acetone bath the structures looked like presented in Fig. 3.2. The exact parameters used in the process are presented in Appendix B.

---

[1] Optical lithography took place in the clean room facility at the WMI. This facility is equipped with standard tools for optical lithography like resist coaters, hot plates, a Karl Süss MJB3 mask aligner and the reactive ion etching system Plasmalab 80 Plus with ICP plasma source (Oxford Instruments Plasma Technology).
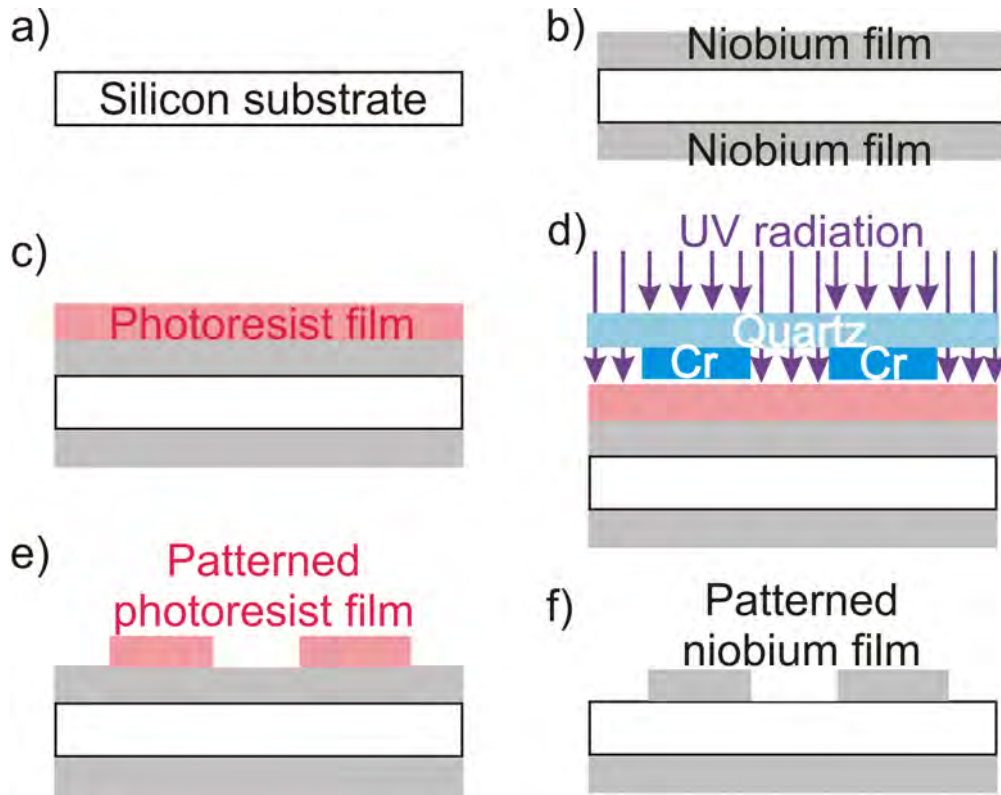
Figure 3.1: Scheme of the sample production process. a) A silicon substrate (white rectangle) is chemically cleaned with acetone and isopropanol in order to remove any kind of organic and ionic impurities [48]. b) A film of niobium (gray rectangle) is sputtered onto the substrate. Since we need a ground plane on the bottom of the substrate, the same process is repeated for the other side of the chip. Subsequently the sample is cleaned in acetone and isopropanol again. c) The thin film of the photoresist (AZ 5214) is spin coated onto the sample. Then the sample is soft-baked. d) The optical mask (black rectangles) is put on the top of the sample using a a mask aligner. The photoresist not covered with the chromium structure on the mask is radiated with UV light. e) Then the sample is put in a photoresist developer. The non-radiated regions of the photoresist film dissolves. The result is the patterned photoresist film. However, before patterning a desired microstrip structure (steps d and e) the thicker edges of the photoresist film resulting from the spin coating process have to be removed. In this manner one assures that the optical mask with the microstrip structure is as close to the photoresist film as possible to avoid diffraction effects. So steps d and e are conducted twice: first for the edges of the photoresist film and then to print the structure. f) The sample is reactive-ion etched (RIE) with Argon and SF_6 in order to remove the metal film not covered by the lack. At the end of the process the resist is dissolved hot acetone.
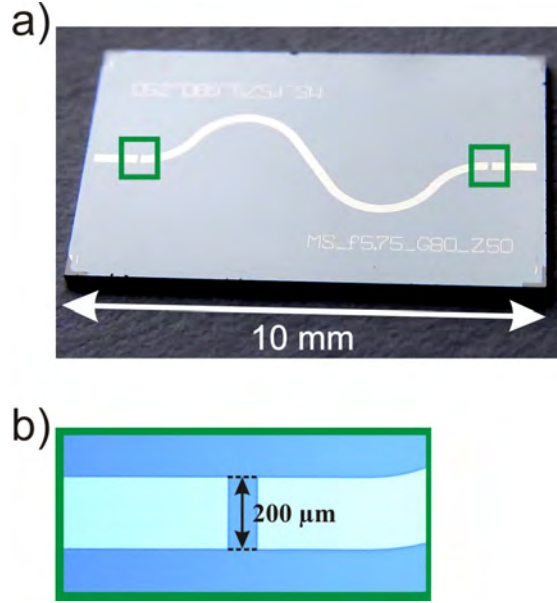
Figure 3.2: Photograph of the sample with the characteristic impedance $Z_0 = 50\,\Omega$. a) The resonator is coupled to the external circuit by the coupling capacitors (green boxes). b) Optical microscope image of the gap capacitor with gap width $g = 80\,\mu m$. For this gap we calculated the corresponding capacitance of 15.8 fF.

Microstrips with constrictions and antennas were fabricated in the same way. In Fig. 3.3b and 3.4b microscope images of a constriction structure and an antenna structure respectively are presented.

3.3   The measurement process

3.3.1   The set-up

We used sample holders made of copper covered with a thin film of gold to avoid oxidation (Fig. 3.1c). They were fabricated by the in-house workshop. The holder has the form of a box with a cavity for the sample milled in the middle of it as well as two holes for the SMA connectors. The galvanic connection between the pins of these coaxial connectors and the feed lines of the sample was realized with conducting silver glue (3.1d). For transmission measurements we connected the box via stainless steel coaxial cables to the vector network analyzer (VNA) HP 8722D. Then the box was mounted in a ^{4}He bath cryostat (cf. Fig. 3.1b). In such a way we measured at 4.2 K. The reduction of the temperature to 1.8 K was done by means of the evaporation cooling method. The Dewar was short-connected to an external pump and the vapor was pumped out. In this way the particles with most energy ware taken away from the system. The calibration of cables and ports of the VNA was done by measuring the

transmission through the connected coaxial cables at 4.2 K and 1.8 K. The scheme of the experimental set-up is presented in Fig. 3.1a.

3.3.2   Transmission measurements

At the beginning of the experimental process a suitable set of parameters for the vector network analyzer (VNA) was chosen. A VNA compares input and output signal and delivers the complex S-parameters. (cf. Section 2.5). The IF bandwidth defines the amount of noise recorded by a receiver [38] together with the actual measurement signal. The lower the IF bandwidth is chosen, the less noise is recorded. Thus we get better results with lower bandwidth. Nevertheless this parameter also influences the measurement time (sweep time). A reduction of the IF bandwidth to half of the original values results in doubling of the sweep time. We compared the results of measurements for two values of the bandwidth: 30 Hz and 300 Hz (Fig. 3.3). Since we saw no relevant difference, we chose the higher value 300 Hz for further measurements.

Using the above presented set-up we measured transmission spectra of resonators between 50 MHz and 18 GHz. As presented in Fig. 3.4 in the vicinity of resonance those spectra exhibit a Lorentzian behavior:

$$S_{21}(f) = \frac{\Gamma/2}{(f - f_0)^2 + (\Gamma/2)^2},\qquad(3.1)$$

where f_0 is the resonant frequency of the resonator. The full width at half maximum Γ is the width of the Lorentz peak at 3 dB attenuation [49]. Thus the data was fitted with a Lorentzian and the loaded quality factor Q_{L} of the resonators was calculated as follows:

$$Q_{\mathrm{L}} = \frac{f_0}{\Gamma}.\qquad(3.2)$$

.

3.4   Simulation of the coupling capacitance

In the theoretical part we presented the *LRC* model, which describes a microwave resonant circuit. The gap between the resonator and external circuits was modeled as a coupling capacitance C_{k}. If C_{k} is large, then the circuit is said to be overcoupled and the loaded quality factor of the circuit is high, the opposite is valid for an undercoupled circuit. Moreover the coupling capacitance determines the position of the resonant peaks.
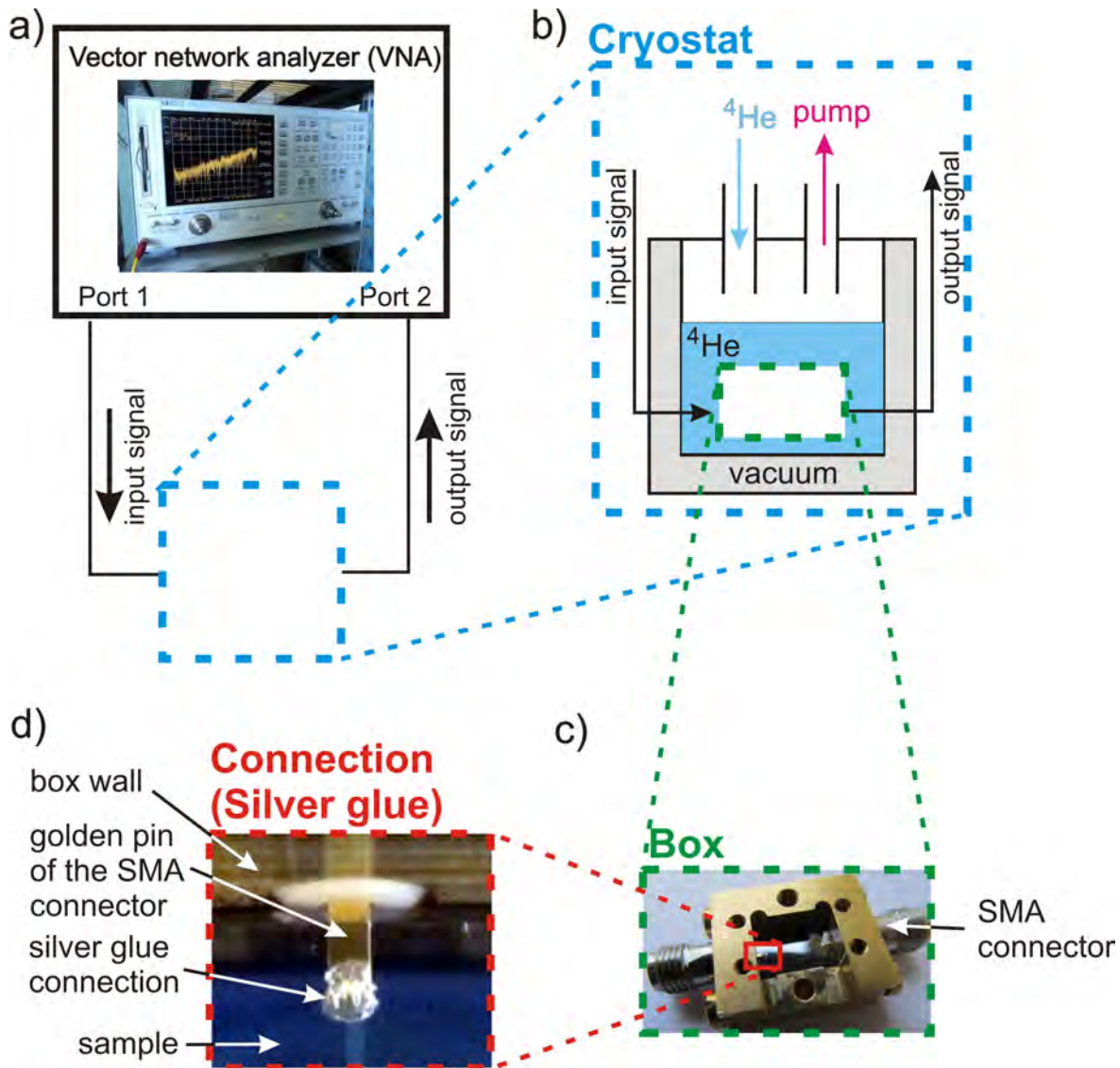
Figure 3.1: Scheme of the experimental set-up for measurements of microstrip resonators at low temperatures (4.2 K and 1.8 K). a) The input signal coming from the first port of the VNA is detected in the second port (yielding the transmission coefficient S_{21}). b) The working principle of a cryostat. The input and output cables are connected to the sample holder (green box). Liquid helium ^{4}He is poured into the Dewar until the sample is fully covered with helium (cooling to 4.2 K). Further cooling is possible by evaporation cooling (magenta arrow). In this way the ^{4}He bath was cooled to 1.8 K. c) The sample holder (box). The pins of SMA connectors are contacted with the transmission line with silver glue (red box). d) The spot of silver glue between the feed line and the pin of the SMA connector.
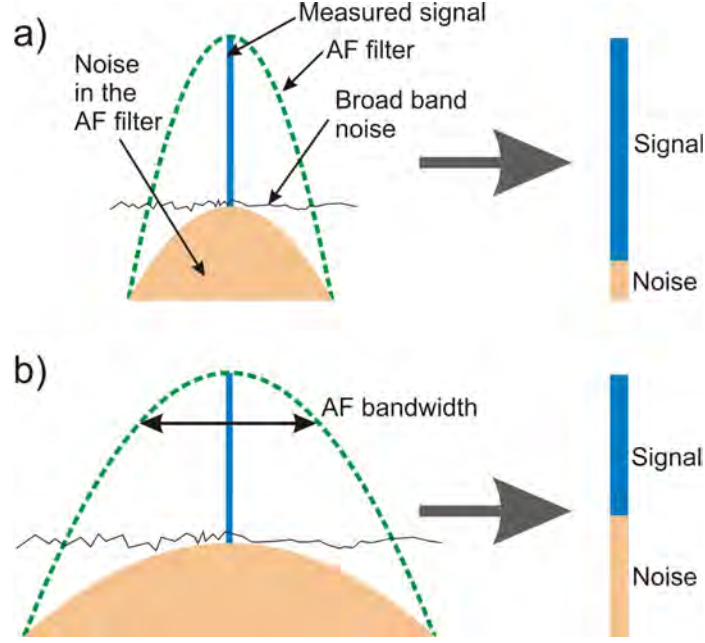
Figure 3.2: IF bandwidth determines the bandwidth of an IF filter. The power density of broad band noise is uniformly distributed over the frequency axis. Thus the larger the bandwidth, the more noise is transmitted to the receiver. The figure was adopted from [38].

The coupling capacitance.is determined by the geometry of the gap between the feed line and the resonator line. Since a future aim is to be able to design resonant circuit with given parameters we have to be able to predict the values of the coupling capacitance for a given gap geometry. That is why we applied the numerical simulation software FastCap2 for this purpose. This tool calculates the capacitances of the distributed element circuits and is thus suitable for the analysis of our microstrip resonators.

In a preliminary attempt the feed lines, the resonator, the ground plane and the dielectric layer were modeled with FastCap2 utilities [50]. We defined a permittivity constant of the dielectric layer as $\varepsilon_r = 11.9$ and the global dielectric constant of air as $\varepsilon_0 = 1$. Large areas were divided into smaller panels (discretization), especially in the vicinity of the edges we increased the density of the discretization (compare Fig. 3.1) [51]. Finer discretization increases the precision of obtained results, however in our case the model became too complex for FastCap2. So we decided to simplify the model.

From the theoretical considerations (compare Section 2.2) we know that the electric field lines spread partially in the air and partially in the dielectric region. So instead of drawing the silicon substrate we defined a global effective permittivity constant which included both the air and the dielectric region. The effective permittivity constants
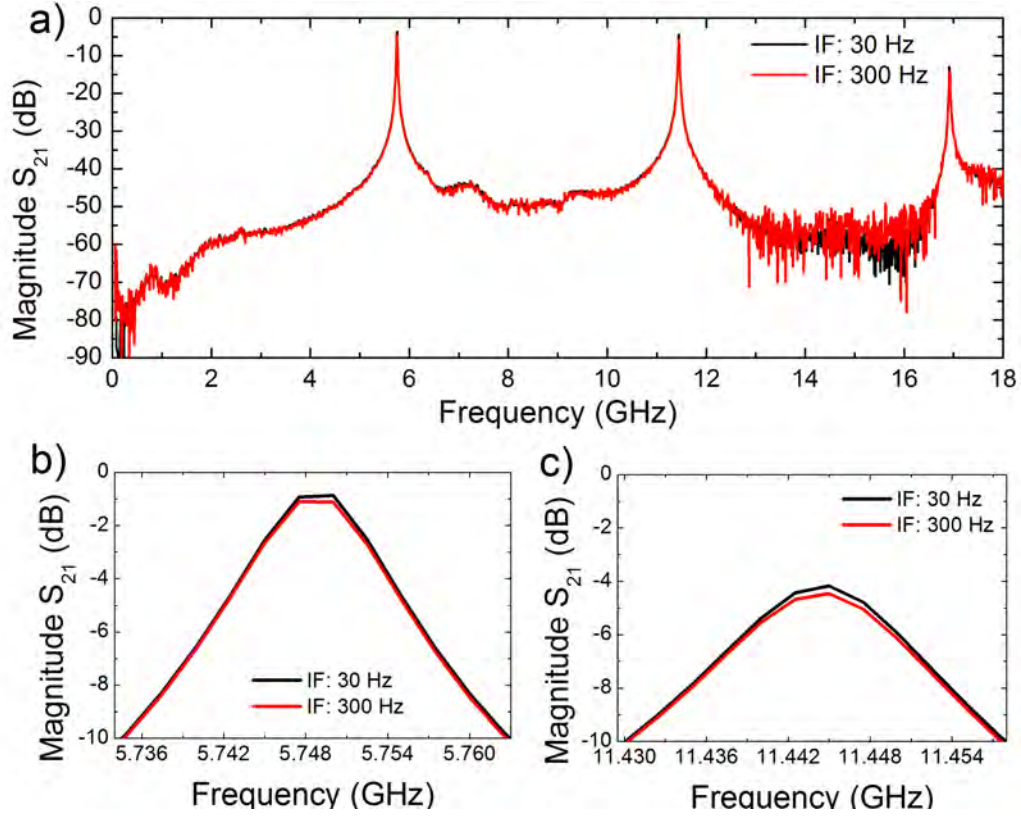
Figure 3.3: Transmission spectra of an overcoupled resonator ($g = 10\,\mu m$, $Q_L = 332$) at the temperature $1.8\,K$ measured with different IF bandwidths. a) Within the measured frequency range three resonant peaks are observed. The resonator acts like a filter transmitting only the signal with frequencies near the resonant frequencies. b) Transmission spectra of the resonator near the first resonant frequency $f_0 = 5.72\,GHz$. c) Transmission spectra of the resonator near the second resonant frequency $f_0 = 11.4\,GHz$.
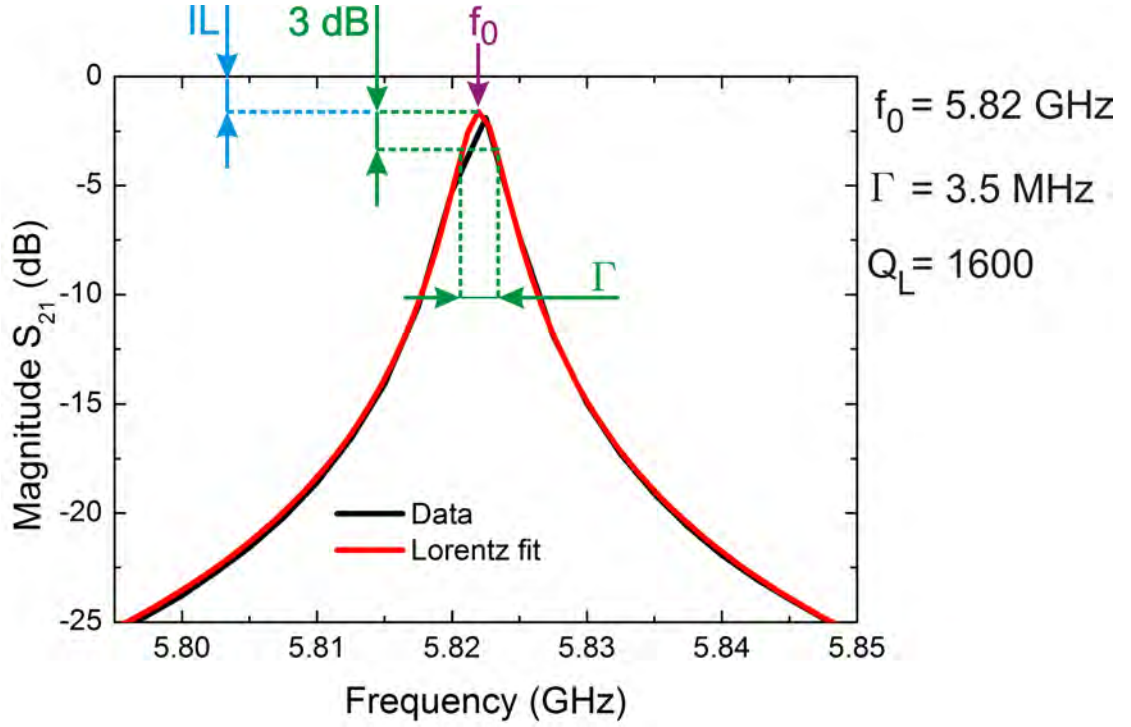
Figure 3.4: The transmission spectrum of a microstrip resonator ($g = 80 \, \mu m$, $Q_{\mathrm{L}} = 1600$) near the first resonant frequency at the temperature $4.2 \, K$. The black solid line is a Lorentz fit to the data points. We marked the resonant frequency position and the full width at half maximum Γ by arrows. The narrower the peak is, the higher the loaded quality factor. Insertion loss IL is defined as the transmission at resonance. For overcoupled resonators insertion loss is very small.
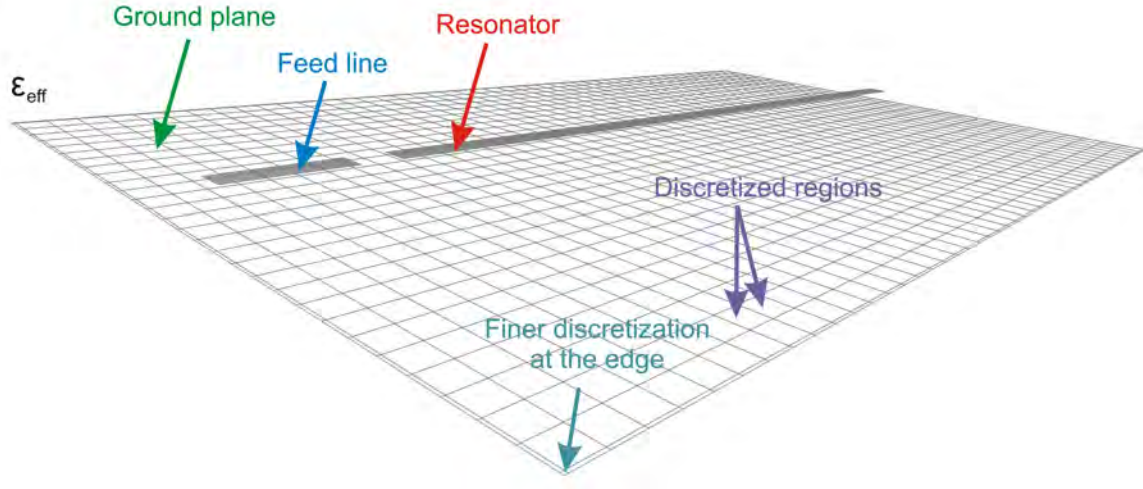
Figure 3.1: The model of the coupling capacitor for simulation purposes. The ground plane, the feed line, the distance between the ground plane and the resonator and the width of the resonator were modeled to scale. To simplify the calculation the resonator was sketched as a straight transmission line. All structures were discretized to improve the precision of the simulation. Additionally the panels of the discretization at the edge were made smaller in order to compensate the fringing fields [52]. Also the feed line and the resonator line were discretized, which is not visible in the figure. A global permittivity constant ϵ_{eff} was defined instead of modeling the dielectric.

used for our simulations are 5.5, 4.5 and 4.9 (compare Section 5.2).

Chapter 4

Experimental results

We have characterized the transmission properties of microstrip resonators designed to a fundamental resonant frequency of 5.75 GHz (cf. Section 3.1) using the vector network analyzer (VNA) HP 8722D. All samples were characterized in a ^{4}He bath cryostat as described in the previous chapter. Since this set-up is less complex than the one for measurements at temperatures of the order of mK, we could measure a relatively large amount of samples efficiently. We studied the influence of the gap width on the position of the resonant frequency, the quality factor and the insertion loss of the microstrip resonators. We also investigated the effect of constrictions and antennas on our circuits. In this chapter we present and discuss the measurement results. The plots show the logarithmic magnitude of the transmission coefficient S_{21} in dependence of the frequency. First we consider spectra of conventional microstrip resonators. Afterwards we analyze the influence of constrictions and antennas.

4.1   Microstrips without constrictions and antennas

In Fig. 4.1 we show a transmission spectrum of an overcoupled microstrip resonator. We can distinguish three resonant peaks for the first three harmonic modes (compare Fig. 3.2). For the resonator the first resonant frequency is $f_0 = 5.72$ GHz, which is in very good agreement with the desired frequency (cf. Section 3.1.1). No parasitic resonances are visible within the measured frequency range (50 MHz - 18 GHz). We can also distinguish the capacitive character of the background spectrum. This is due to the fact that we applied gap-coupling of our resonators. A gap between the transmission lines acts like a coupling capacitance (cf. Section 3.1).
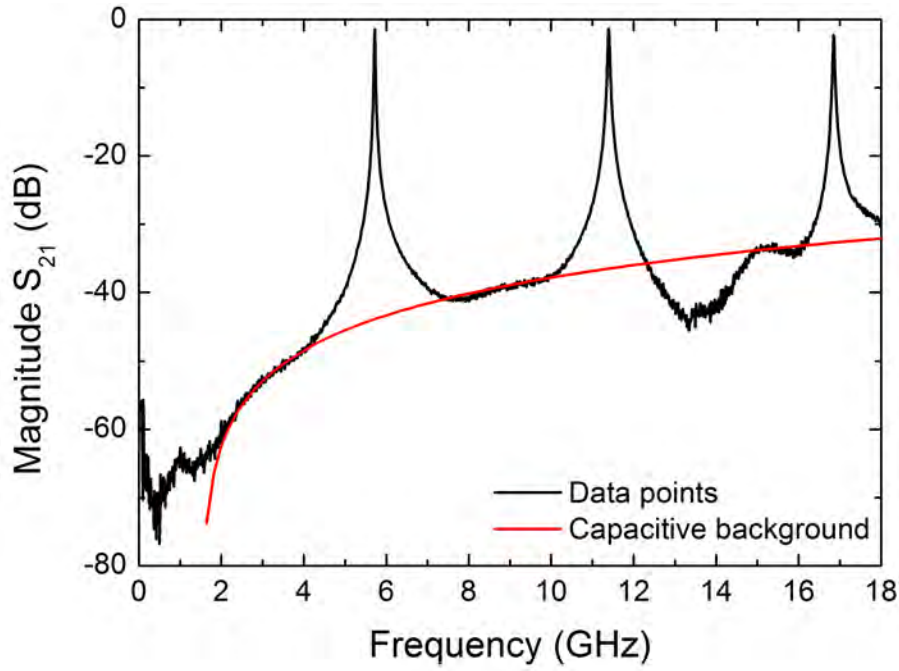
Figure 4.1: Transmission spectrum of an overcoupled microstrip resonator with a gap width of $5\,\mu\mathrm{m}$ (loaded quality factor $Q_\mathrm{L} = 206$) measured at $4.2\,\mathrm{K}$ with an IF bandwidth of $30\,\mathrm{Hz}$ and a VNA output power of $-10\,\mathrm{dBm}$. The spectrum is a composition of a capacitive background and resonant peaks of Lorentzian form. The capacitive background spectrum was calculated with a model of a terminated lossless transmission line from [24]. With this model we have found a dependence of the background spectrum on the frequency f of the form $\frac{f}{\sqrt{1+f^2}}$.

4.1.1 Power and temperature dependence

Power dependence First we analyzed the response of our resonant circuits to the change in the input power $P_{\text{resonator}}$. For this purpose we varied the power P[1] at the output of VNA. The results are shown in Fig. 4.2. We observe no change in the position of the resonant peaks for different powers P. Also the width of the peaks at the attenuation of -3 dBm remains the same.

To explain this effect let us reconsider the Two Level Systems (TLS, compare Subsection 2.4.1) [35]. Those are states in the dielectric substrates of the considered microstrips which interact with the charge carriers and in this the energy is dissipated. They are the main sources of losses in the dielectric layer.

Now let us evaluate an average photon number $\bar{n}$ in our resonator. Assuming the attenuation of our cables to be 1 dB [54], the power P of -10 dBm corresponds to the $P_{\text{resonator}}$ of 80 µW. We apply the formula [55]

$$P_{\text{resonator}} = \bar{n}\hbar\omega_0\Gamma, \tag{4.1}$$

where ω_0 is the first angular resonant frequency and Γ is the full width at half maximum. We get average photon numbers of 10^{12}, 10^9 and 10^6 for the three values of the power at the output of the VNA. At such a large number of photons all TLS are saturated. This is the reason why we did not observe a power dependence of the characteristics of our resonators in this range.

Temperature dependence First we have characterized our resonators at the temperature of 4.2 K. For seven of the resonators we additionally performed an evaporation cooling to the temperature of 1.8 K (cf. Subsection 3.3.1). In Fig. 4.3 we show a comparison of the results for a microstrip with a gap width of 10 µm. We see a frequency shift to lower frequencies for lower temperatures. The displacement is about 2 %. We observe the same dependence for other characterized resonators (cf. Table 4.1). Additionally a slight increase of quality factors at lower temperatures can be seen. The order of magnitude of the discussed changes is rather small, however it occurs for all measured samples. The samples were measured in one cooldown, so we can exclude the effects of the sample holder and silver glue on this issue.

We consider two possible origins of the described effects. The frequency is proportional to $\frac{1}{\sqrt{L}}$ [56], where L is the inductance of the resonator (cf. Section 2.3). The

---

[1]The power P at the output of the VNA is specified in units of dBm [53], where $P(\text{dBm}) = 10\log\left(\frac{P(\text{mW})}{1\text{mW}}\right)$.
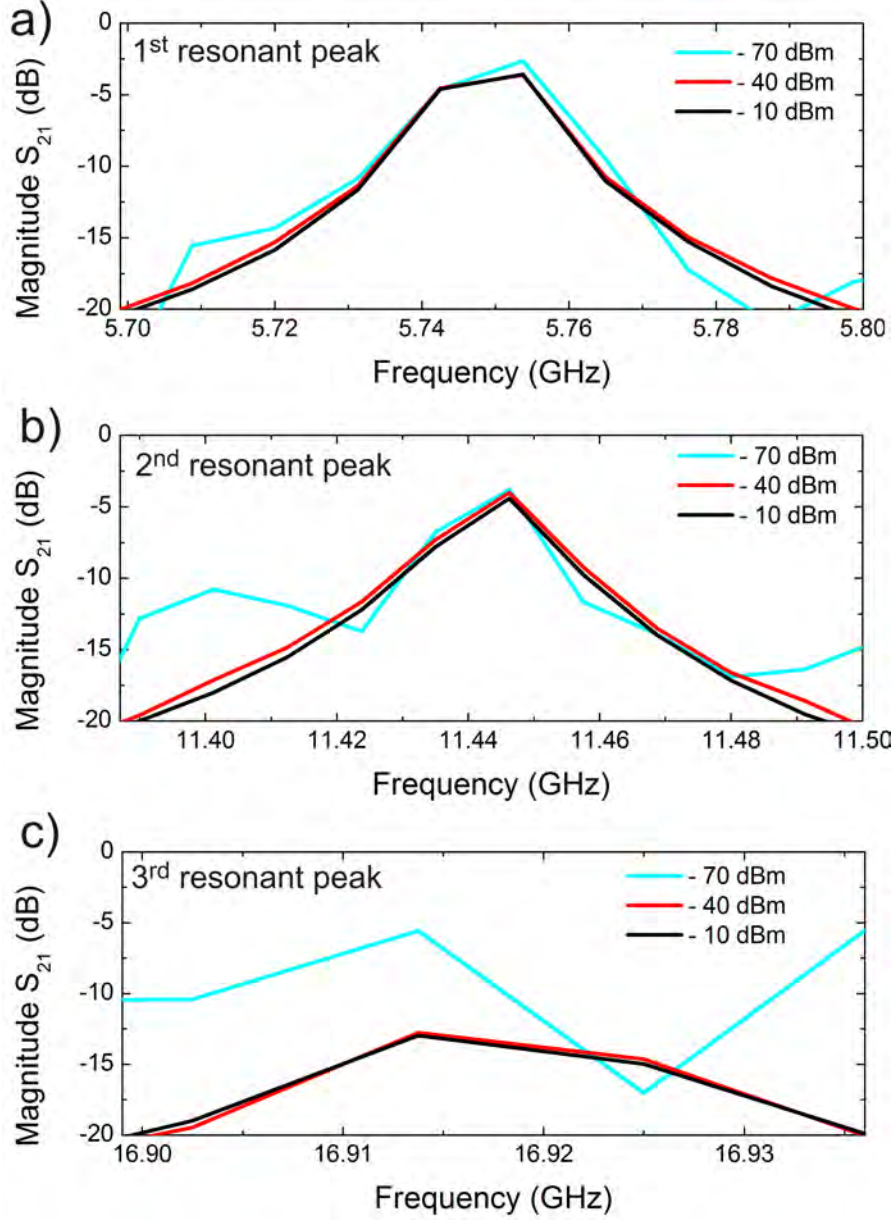
Figure 4.2: Transmission spectra of a microstrip resonator with the gap width of $10\,\mu m$ $(Q_{\mathrm{L}} = 332)$ recorded at different powers P at the output of VNA. We observe no change in the peak structure and its position as the power decreases. We see no third resonant peak for $P = -70\,\mathrm{dBm}$, due to the bad signal-to-noise ratio. We chose the highest power $(P = -10\,\mathrm{dBm})$ for all further measurements.

g (µm)	Z_0 (Ω)	f_0 (GHz) [4.2 K]	f_0 (GHz) [1.8 K]	Q_L [4.2 K]	Q_L [1.8 K]
5	50	5.7173	5.7164	260	262
10	50	5.7498	5.7487	432	437
20	50	5.7758	5.7750	556	562
80	50	5.8220	5.8212	1640	1750
5	70	5.9095	5.9094	611	623
10	70	5.9321	5.9311	570	578
20	70	5.9504	5.9494	697	709

Table 4.1: Comparison of the measurements of seven microstrip resonators at temperatures 1.8 K and 4.2 K. We present resonant frequencies f_0 and loaded quality factors Q_L for microstrip resonators with characteristic impedances Z_0 of 50 Ω and 70 Ω with different gap widths g.

inductance L is a sum of the temperature independent kinetic inductance L_g and the temperature dependent kinetic inductance $L_k(T)$ [13]. The kinetic inductance scales as $L_k \propto \lambda(T)^2$, where $\lambda(T)$ is the temperature dependent London penetration depth [57]. The same frequency dependence was observed by Peter K. Day *et.al.* [56] and David I. Schuster [31]. However according to Day the quality factor should have decreased for lower temperatures. We do not know the reason for the observed temperature dependence of the quality factor.

The second considered origin of the observed effects are TLS. In [35] David P. Pappas *et.al.* have also described an observed decrease in resonant frequency for the decreasing temperature. However, we expect at the examined temperatures, that all TLS are saturated. Therefore they do not contribute to the dielectric losses in the resonator. Additionally for increasing temperatures the TLS should saturate. As a result the quality factor should increase for higher temperatures. This is not our observation. Therefore the TLS cannot explain the behavior of the quality factors as well.

4.1.2   Gap width dependence of resonators with a characteristic impedance of 50 Ω

We have characterized eight microstrip structures with gap widths ranging from 5 µm to 640 µm. We show the results in Fig. 4.4. Let us analyze the effect of an increase in the gap width on the spectra of the resonators. First the peaks get shifted to higher frequencies and we observe a decrease in the width of the curves. Moreover the insertion loss at the resonant frequency increases. Those changes are indications that our microstrip resonant circuit changes from the overcoupled to the undercoupled one
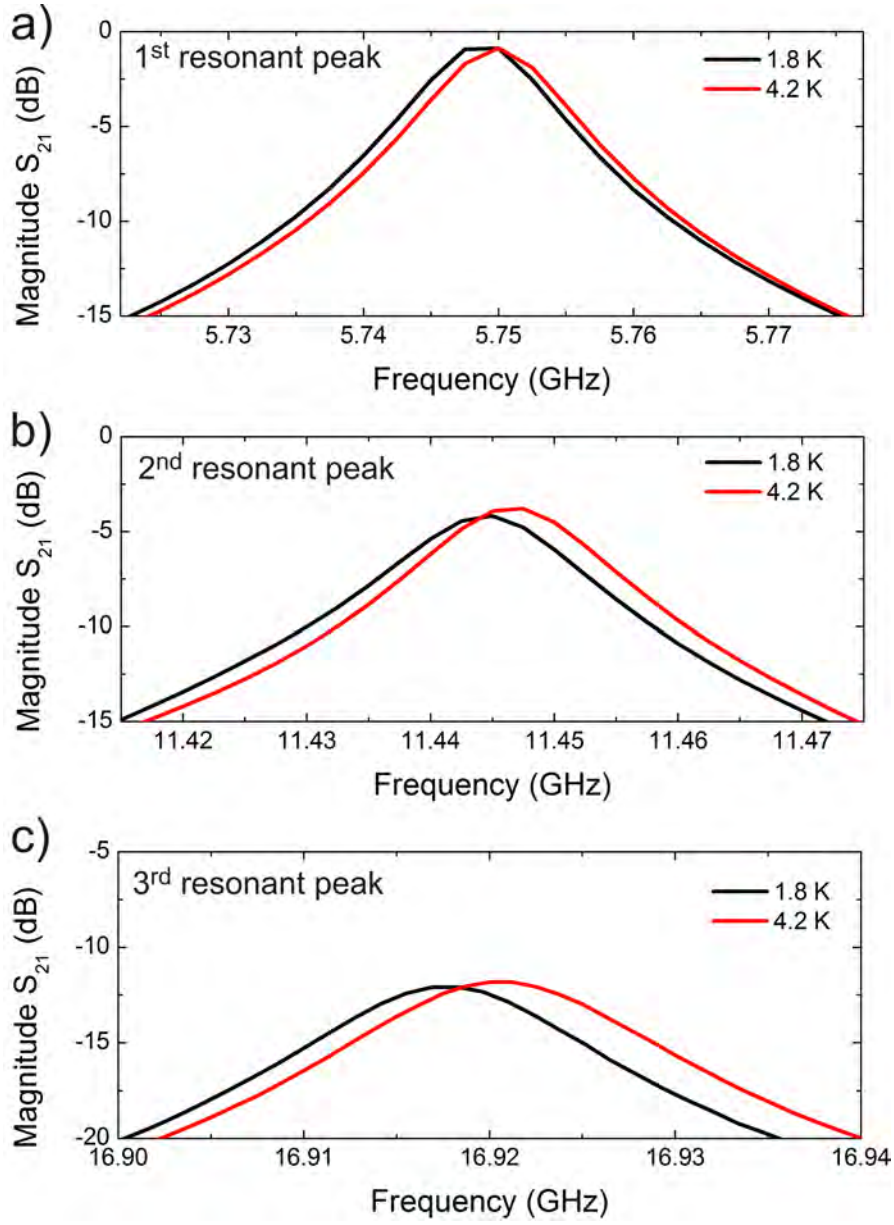
Figure 4.3: Transmission spectra for a microstrip resonator with the gap width of 10 μm recorded at different temperatures. The peaks show a shift to lower frequencies for the lower temperature. This effect is described in the text and in [35].

(compare the theoretical discussion in Section (2.3.2)). For the resonator with the gap width of 640 μm we have not observed any resonant peaks. This is probably due to the fact that those peaks have a very high insertion loss. When the insertion loss of a resonator approaches the order of magnitude of the noise signal, we are not able to distinguish the peaks.

4.1.3 Gap width dependence of resonators with a characteristic impedance of $70\,\Omega$

The feed lines of the considered resonators have the characteristic impedance of $50\,\Omega$. In the previous section, we have shown the resonant peaks of the resonators with the characteristic impedance of $50\,\Omega$.

To examine the influence of the the resonator's characteristic impedance, we have performed the same measurement as described in the previous section also for resonators with a characteristic impedance of $70\,\Omega$ (compare Fig. 4.6). The impedance of the feed lines was kept constant. We present the results in Fig. 4.5. Let us compare whether the results agree quantitatively.

When the values of the gap width become larger we observe a shift of the peaks to higher frequencies, just like it was in the previous case. For the resonator with the largest gap width the frequency is too low. We do not know the reason for this. Considering now the width of the peaks we see the same tendency as before: the peaks get narrower for larger gap widths. For the resonator with the gap width of 40 μm the peak is unexpectedly too narrow.

Let us now turn to the insertion loss. For the first resonant peak (Fig. 4.5a) we observe a similar behavior as for the resonators with a characteristic impedance of $50\,\Omega$, where the insertion loss increased with larger gap width. For the second and third peak the values of the insertion loss scatter.

The discussion can be summarized as follows. In general we see the same response of the circuit to the change of the gap width. Some data do not suit to the previously found relations. We do not know the reason for this.

4.1.4 Variation of the characteristic impedance

We have analyzed a microstrip with the gap width of 20 μm. A change in the characteristic impedance Z_0 was realized as a change of the width of the resonator line (compare Fig. 4.6). We varied the width of the resonator line between 679 μm (for characteristic impedance $Z_0 = 25\,\Omega$) and 23 μm ($Z_0 = 100\,\Omega$). The measurement results are shown in Fig. 4.7. We see a shift of the peaks to higher frequencies for higher
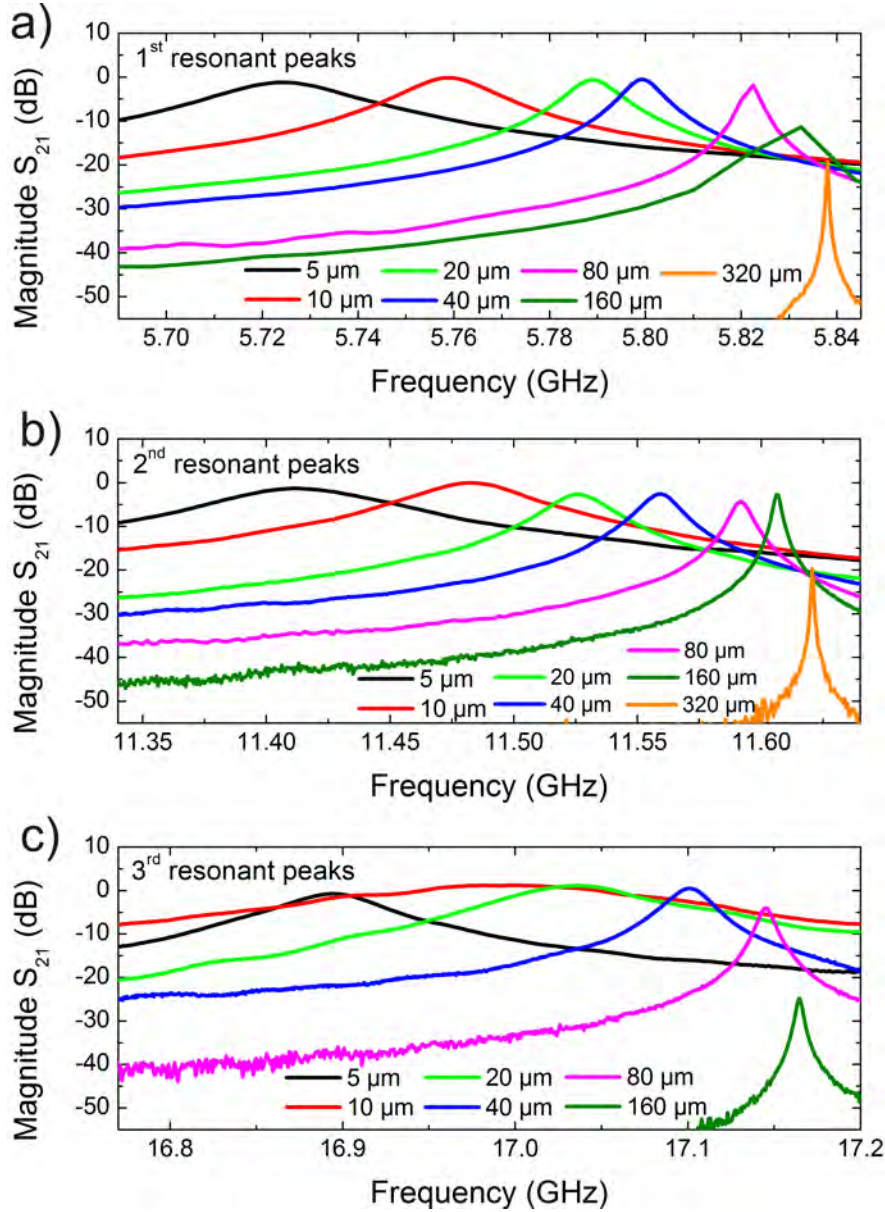
Figure 4.4: Resonant peaks of a series of microstrip resonators with different gap widths and a characteristic impedance of $50\,\Omega$. The peaks show a shift to higher frequencies for larger gap widths. Also the form of the peaks changes. The third resonant peak of the resonator with the gap width of $10\,\mu m$ is wider than expected. Our explanation is an error in the calibration for this frequency. For the resonator with gap width of $320\,\mu m$ we have not observed the third resonant peak. We do not know the reason for this.
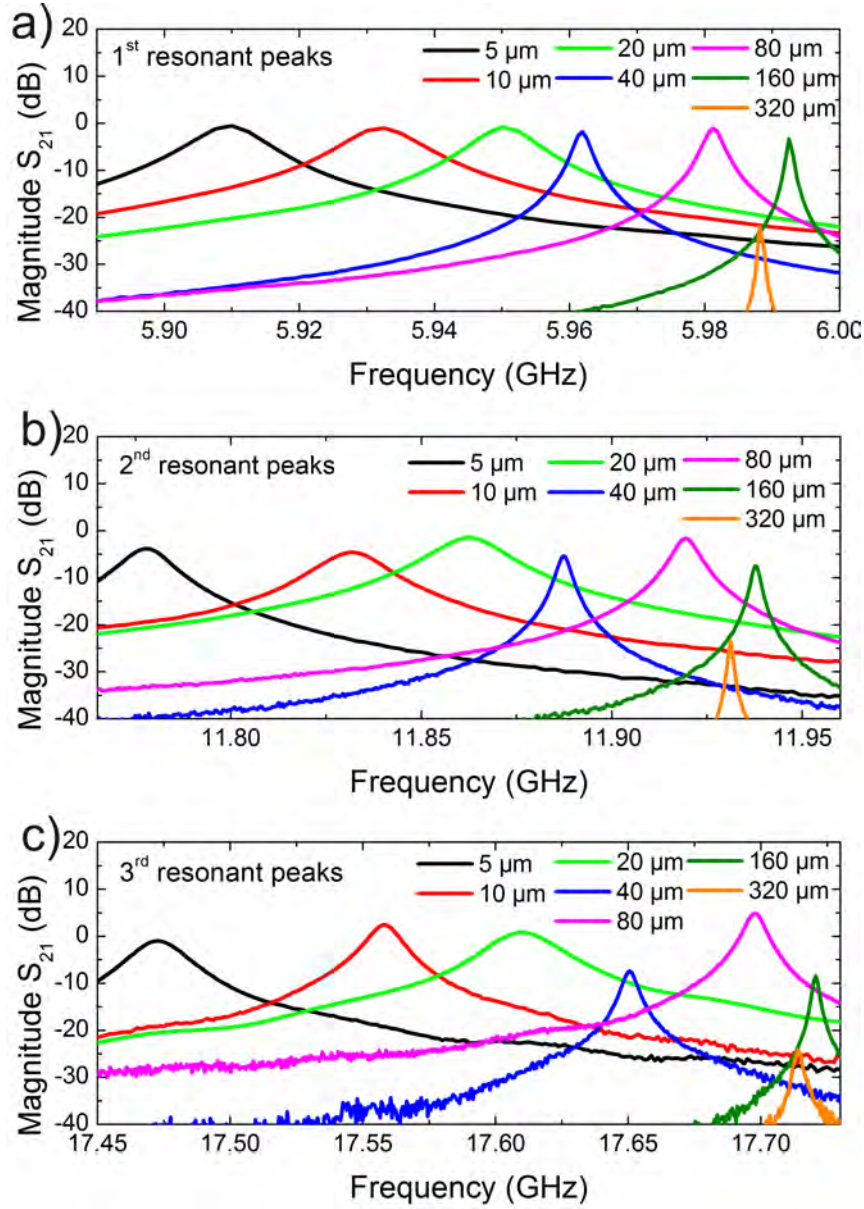
Figure 4.5: Resonant peaks of microstrips with a characteristic impedance of the signal line of $70\,\Omega$. We varied the gap width and compared the resulting response with the one of microstrips with a characteristic impedance of $50\,\Omega$ presented in Fig. 4.4.
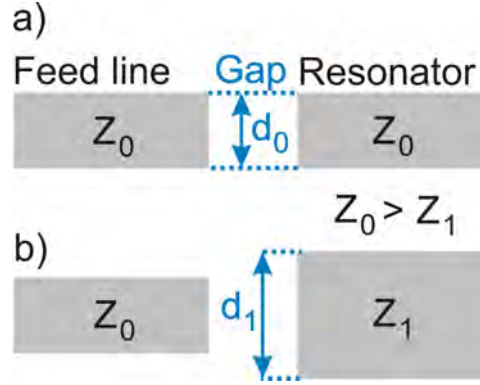
Figure 4.6: Schematic drawing of the gap between the resonator and the feed line. a) The resonator and the feed line have the same width d_0, which corresponds to the characteristic impedance Z_0. b) When the width of the resonator is increased to d_1, the characteristic impedance decreases.

Z_0 (Ω)	f_0 (GHz)	Q_L
25	5.49	582
45	5.73	528
50	5.78	556
60	5.87	579
70	5.95	697
100	6.10	1270

Table 4.2: Resonant peaks and loaded quality factors for microstrips with different characteristic impedance Z_0. We can see a rise in the resonant frequency f_0 with larger impedance. For the first four microstrips the values of the quality factor scatter. However we can see a significant increase for the two resonators with the largest characteristic impedance.

characteristic impedance. In order to analyze the reaction of quality factors let us look at Table 4.2. For the first four lower values of Z_0 the data scatter. However we can observe a considerable rise of the quality factors for the two highest values of the characteristic impedance.

We now discuss this behavior. Let us analyze the gap presented in Fig. 4.6. Considering a simple model of a parallel plate capacitor, if we increase the width of one plate, we also increase the coupling capacitance. As predicted by theory (Equations (2.8) and (2.10)) we should then observe a drop in the resonant frequency, which we do see indeed.

The second aspect is the quality factor. Let us look at the equation

$$Q_\mathrm{L} = \frac{\alpha}{\beta/Z_0 + \gamma}, \tag{4.2}$$

which can be derived from Equations (2.8), (2.7) and (2.9) from the theoretical part.
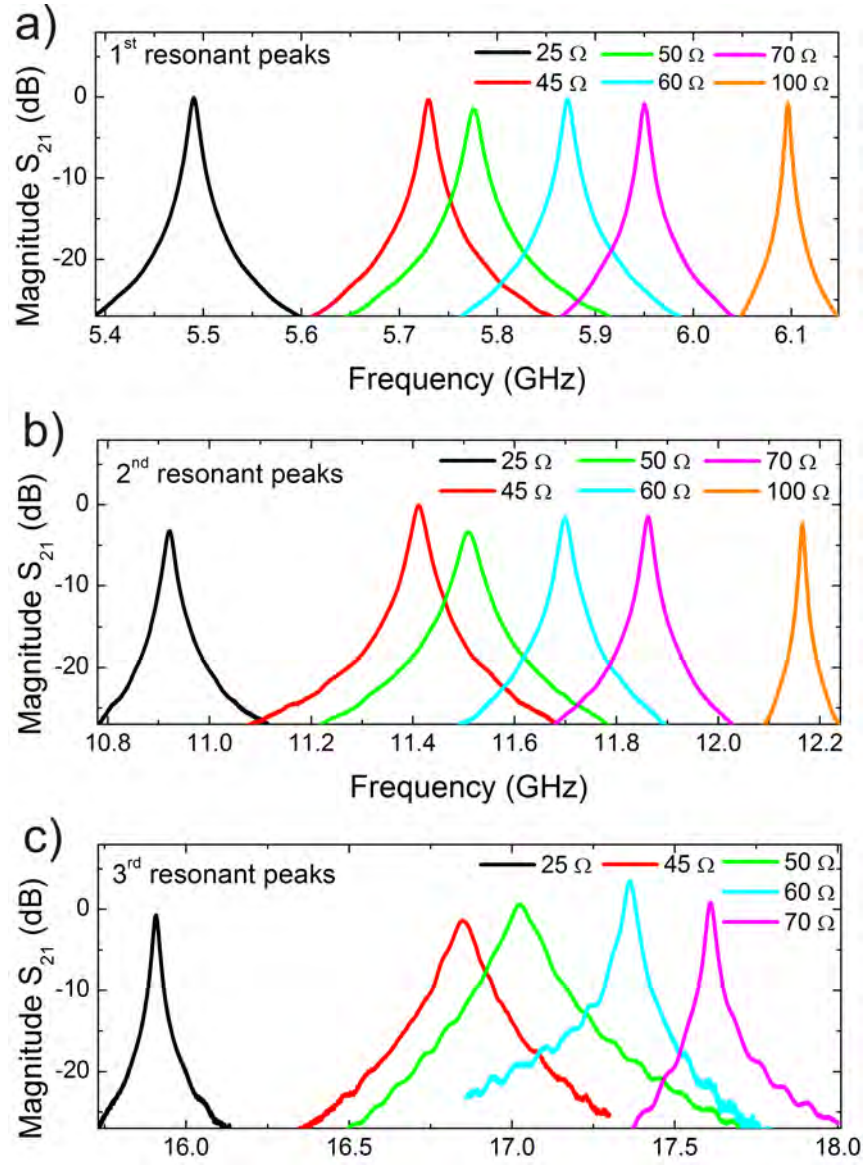
Figure 4.7: Resonant peaks of a set of microstrip resonators with different characteristic impedance of the signal line. All microstrips show a shift to higher frequencies for larger characteristic impedance.

It describes the dependence of the quality factor on the characteristic impedance Z_0. The values α, β and γ are resonator specific parameters depending on the resonant frequency, the capacitance and the resistance of the resonator line. As a result, we should observe an increase in the loaded quality factor with increasing characteristic impedance. This is verified by the results of our experiments as presented in Table 4.2.

4.1.5   The influence of the microstrip geometry

All the microstrip resonators discussed in the previous sections had a geometry like the one depicted in Fig. 4.8a. For this structure we have maximized the bending radius of the line to reduce the parasitic modes of the resonator [58]. However, to implement a constriction we needed a different structure.

Constrictions are used for galvanic coupling of the resonator to qubits (cf. Subsection 3.1.2). For the convenience of the qubit production process the segments of the transmission like should be either horizontal or vertical. That is why we have modified our structure as shown in Fig. 4.8b. The effective length of the line (compare Section 3.1.1) was kept constant.
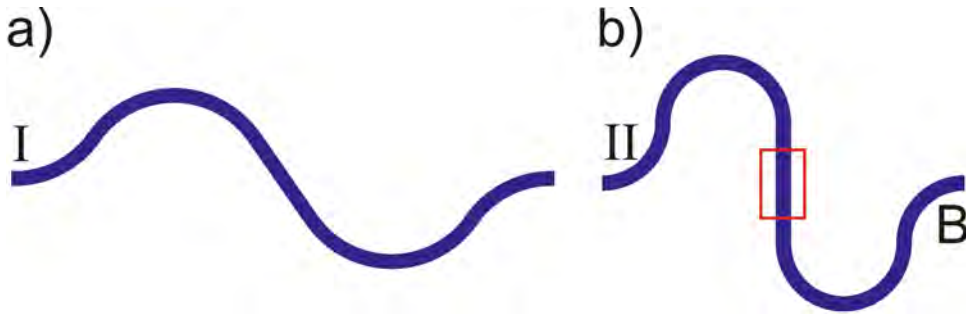

Figure 4.8: Layout of two microstrip structures we used. The first structure (I) was used for all measurements without constrictions and antennas. The line is designed to maximize the bending radius, which avoids cross talk between the microstrip modes [58]. However, in the E-Beam Lithography process for the production of qubits [29], a segment of the line which is either vertical or horizontal is required. So by keeping the length of the microstrip resonator constant we changed the geometry of the line (II) to obtain a vertical segment (red box) of the line.

Structure	Gap width (µm)	f_0 (GHz)	Q_L
I	80	5.82	1640
II	80	5.91	2180
I	320	5.84	19000
II	320	5.92	20000

Table 4.3: Comparison of the results for different microstrip geometries as presented in Fig.4.8. We see an increase in the resonant frequency f_0 and in the quality factor Q_L for the structure 'II'.

In this section we compare the results for both structures. We refer to the first and the second structure as 'I' and 'II' respectively. In Fig. 4.1 we have already presented a spectrum of a microstrip resonator with the structure 'I'. We could see resonant peaks of Lorentz shape and no parasitic modes were present. Now let us look at a spectrum of a microstrip resonator with the structure 'II' in Fig. 4.9. At the transmission magnitude of $-40\,\mathrm{dB}$ there are parasitic modes present. However the magnitude of those parasitic modes is much lower then the magnitude of the resonant peaks.

In Table 4.3 we show the comparison of the characteristics of our circuits for both structures. We observe an increase in the resonant frequency as well as in the quality factor for the structure 'II'.

4.2 Microstrips with constrictions

We have measured the influence of constrictions in the middle of the transmission line on the characteristics of our microstrip resonators. We have examined resonators with the gap width of $80\,\mathrm{µm}$ and $320\,\mathrm{µm}$. The reason for this choice of microstrips was that the resonator with the gap width $80\,\mathrm{µm}$ is overcoupled, but has a relatively high quality factor of 1600 and the resonator with gap width $320\,\mathrm{µm}$ has the largest measured value of the quality factor (19000). In each case we have produced different constriction widths. The narrowest constriction was $2\,\mathrm{µm}$ and the widest $100\,\mathrm{µm}$.

Let us first compare the spectrum of the resonator with a constriction width of $2\,\mathrm{µm}$ presented in Fig. 4.2 to the spectrum of the resonator with the same geometry, but without constriction (Fig. 4.9). Both spectra show resonant peaks and some parasitic modes. An important fact is that the constriction did not introduce any additional parasitic modes to the resonator.

Now let us analyze the resonant peaks of microstrips with different constriction widths in Fig. 4.3. We see a shift of the resonant peaks to lower frequencies for narrower constrictions. In Table 4.4 we show a comparison of the results for the non-constricted
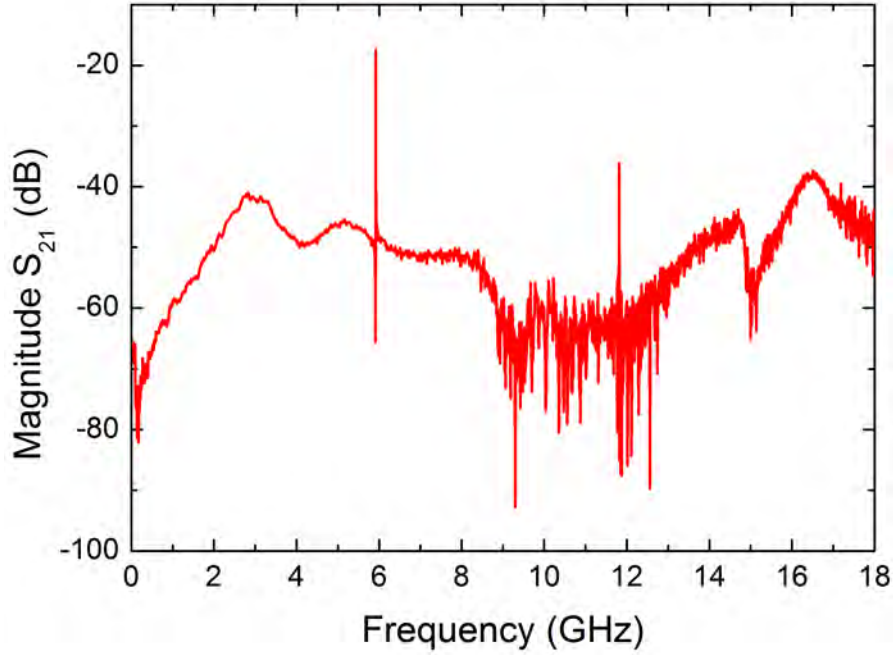
Figure 4.9: Transmission spectrum of a microstrip resonator with the gap width of 320 µm (loaded quality factor $Q_{\mathrm{L}} = 19000$) and the structure 'II' as described Fig.4.8. We see two resonant peaks. The peaks have an asymmetric form. Instead of a Lorentz form the curve has a dip-peak structure (cf. Fig. 4.3). This is most probable due to the reflection at the silver glue connection [59]. We can also see some parasitic modes at the attenuation level of $-40\,\mathrm{dB}$. But those modes do not affect the resonant frequency of our resonators neither its quality factor.

Figure 4.1: A model we apply for the prediction of the behavior of a microstrip resonator with a constriction. For the purpose of simplicity we assume a microstrip resonator line with characteristic impedance Z_0 is interrupted by a constriction with a characteristic impedance Z_1. The total impedance of the microstrip transmission line is $(Z_{\mathrm{total}})^{-1} = \frac{1}{3}\left(2Z_0^{-1} + Z_1^{-1}\right)$. This simple model explains the reaction of our resonator on a change of the constriction's width c. If c decreases, then the impedance Z_1 of constriction increases and the total impedance Z_{total} of the line also increases. From the formulas presented in [24] and in our theoretical part we get the relation $\omega_0 = \frac{\pi^2}{4C^2 Z_{\mathrm{total}}^2}$ between the resonant frequency $\frac{\omega_0}{2\pi}$, the capacitance of the resonator line C and Z_{total}. So we expect a shift to lower frequencies for a narrower constriction.
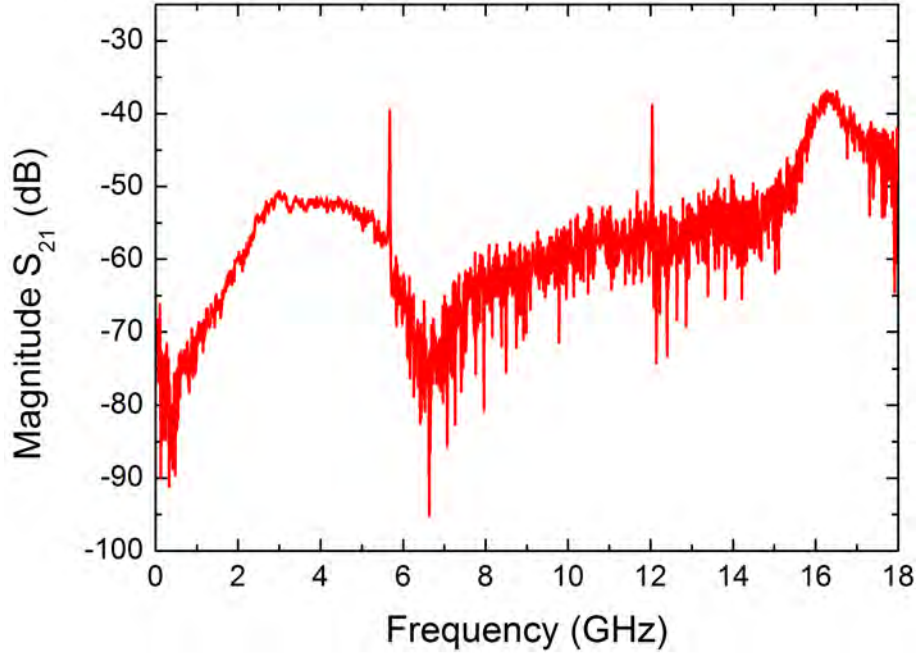
Figure 4.2: Transmission spectrum of a microstrip resonator with the gap width of 320 μm and a 2 μm wide constriction. We see two resonant peaks. In comparison with Fig. 4.9 we see no effect of the constriction on the spectrum of the microstrip resonator.

and constricted microstrip resonators. We observe an increase in the quality factor with decreasing constriction width.

For an explanation of the observed behavior let us apply a simple model of a constriction as presented in Fig. 4.1. A constriction yields a change of the characteristic impedance of the line. Our model explains the dependence of the resonant frequency on the constriction width well.

We also apply this model for the consideration concerning the quality factors. Let us refer to Equation (4.2). With this relation we can again explain the increase of the quality factors for narrower constrictions.

To summarize, the results of this experiment are very promising for the application of the microstrips in the field of circuit QED. Constrictions did not cause a decrease in the quality factor of our resonators. We have even measured higher quality factors for narrower constrictions. Moreover constrictions did not introduce any spurious modes to the microstrip circuit.
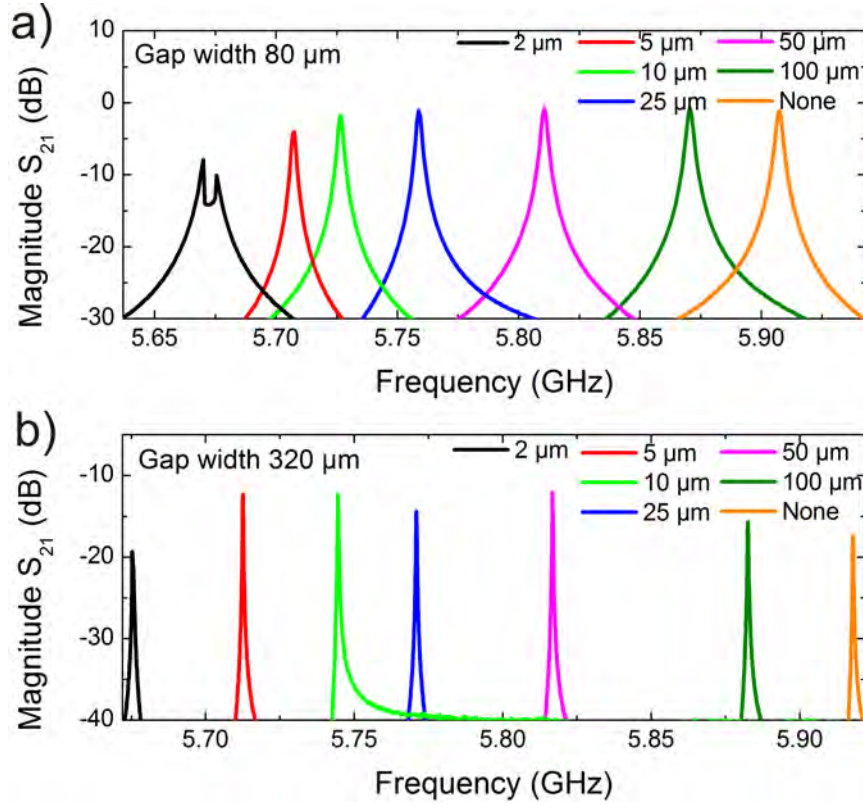
Figure 4.3: First resonant peaks of a set of microstrip resonators with different constriction widths. We see a shift of the peaks to lower frequencies for narrower constrictions. For the microstrip with the gap width of 80 µm and the narrowest constriction the peak has split. We do not know the origin of this effect. For the resonators with the gap width of 320 µm we observe a dip-peak structure of the curves (cf. Fig. 4.9).

Constriction width (µm)	Gap width 80 µm		Gap width 320 µm	
	f_0 (GHz)	Q_{L}	f_0 (GHz)	Q_{L}
200 (no constriction)	5.91	2180	5.92	20000
100	5.87	2220	5.88	16900
50	5.81	2340	5.82	23900
25	5.76	2260	5.77	19400
10	5.73	2690	5.74	20900
5	5.71	2940	5.71	23100
2	5.67	-	5.68	10400

Table 4.4: Results for the resonators with constrictions. We see an increase in the quality factor for narrower constrictions. We also observe a shift of the resonant frequencies to lower values, when the constriction width decreases. For microstrip with the gap width of 320 µm for the narrowest constriction we measured a surprisingly small quality factor. For this peak the full width at half maximum is 544 kHz. Since our frequency resolution is 60 kHz we measure only eight points for this peaks. So this might be a resolution problem. For the microstrip with gap width of 80µm with the narrowest constriction we observed a peak splitting (cf. Fig.4.3) We thus could not calculate the loaded quality factor, due to the unsuccessful Lorentz fit.

Configuration	f_0 (GHz)	Q_{L}
Fig. 4.1b	5.92	1070
Fig. 4.1c	5.90	894
Fig. 4.1d	5.97	1750
Fig. 4.1e	6.02	1430
Fig. 4.1f	5.88	418

Table 4.5: Results of our measurements for the structures presented in Fig. 4.1. The discussion of the results is in the text.

4.3 Microstrips with antennas

Introducing an antenna changes the electrical surrounding of the microstrip. We have investigated the influence of antennas in different configurations (cf. Fig. 4.1[2]) on the microstrip resonator characteristics. The antennas were $50\,\Omega$ impedance matched CPW transmission lines. In Table 4.5 we present the results for our structures.

For single antennas (structures 'A', 'B', 'C') we observe a frequency scattering of $1\,\%$. We see a significant rise in the quality factor for the narrow antenna (structure 'C').

For two antennas (structures 'D', 'E') we observe a frequency variation of $2\,\%$. For the structure 'E' we see a drastic fall of the quality factor. We do not have an explanation for this fact. The comparison of the resonant peaks is presented in Fig. 4.2. We cannot identify any dependence between the different configurations of antennas and the characteristics of the resonator.

---

[2]In this figure antennas are sketched larger than in the real structures (compare Fig. 3.4)
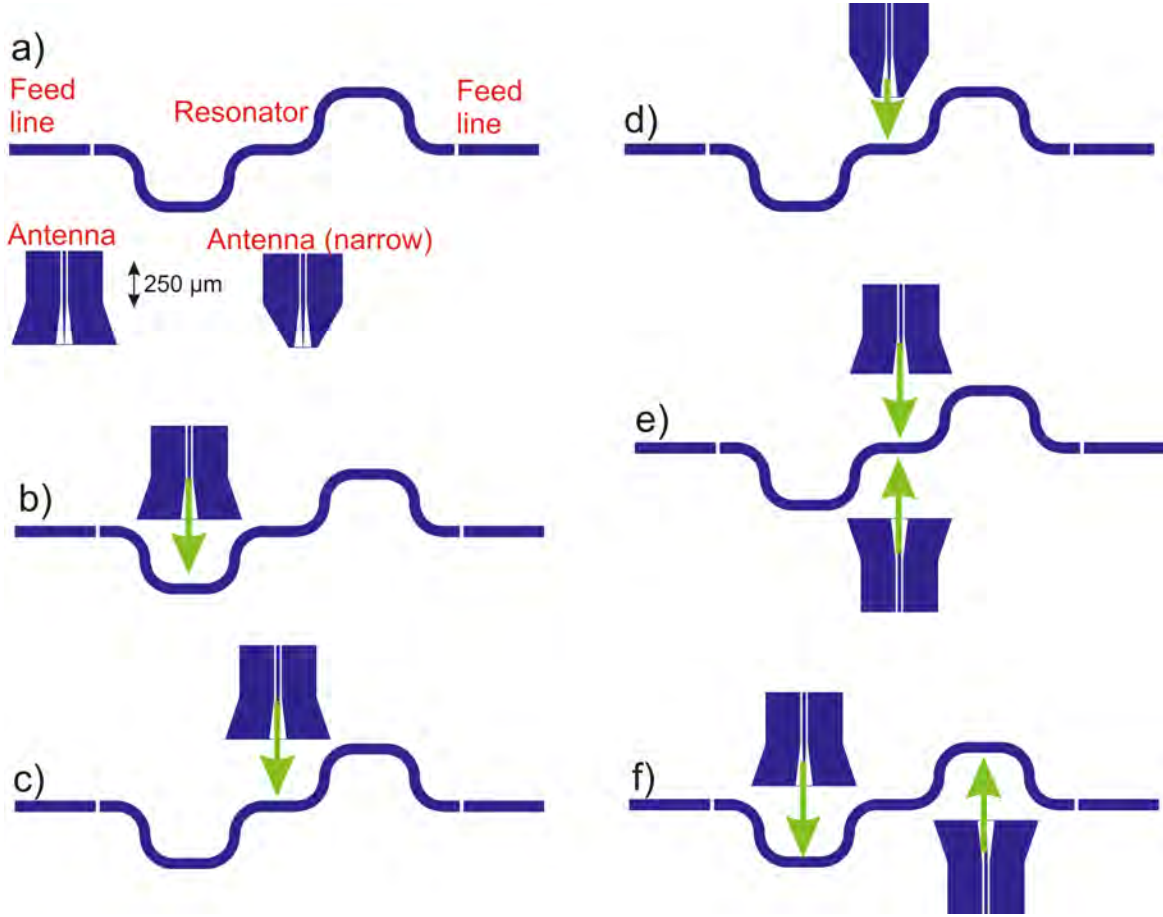
Figure 4.1: Schematic drawings of the configurations we used to measure the influence of antennas on spectra of microstrips. The drawings are not to scale. Antennas are placed in the vicinity of the microstrip line at positions which enable them to interact with different modes of the resonator (cf. Section (3.1.2)). Green arrows indicate positions of antennas. We have examined the influence of conventional CPW antennas on the microstrip resonator (b, c, e, f). Additionally we have designed an antenna with a narrower end (d). a) Antennas are supposed to influence the qubit structures as described in Section (3.1.2). The production process of the qubits requires vertical or horizontal transmission lines as explained in the Section 4.1.5. So we changed the geometry of the resonator line (a) in comparison to the previous microstrips (cf. Fig. 4.8).
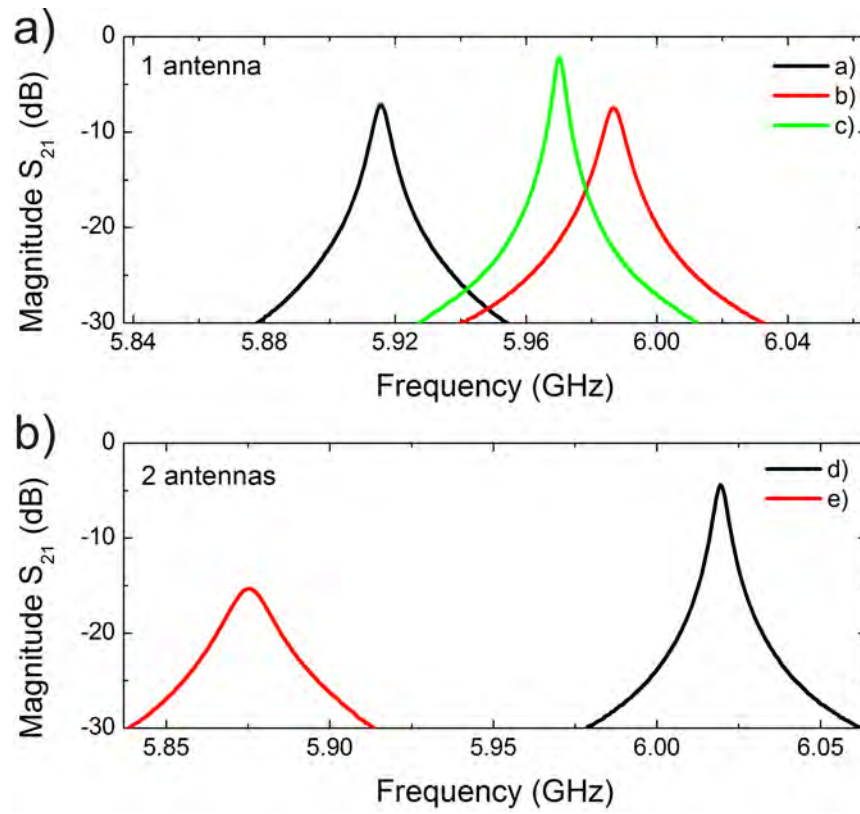
Figure 4.2: Resonant peaks of a set of microstrip resonators with antennas in different configurations from 'A' to 'E' as described in Fig. 4.1. We see a change of the resonant frequency and the form of the peaks for different configurations.

Chapter 5

Analysis

In Chapter 4 we have presented the measured transmission spectra of our resonators. We have also discussed and analyzed the results. In this chapter we show a detailed analysis of the influence of the gap width on the resonator's behavior. We also evaluate the coupling capacitance for our resonators. In the last section of this chapter we compare the measurement results with the theoretical prediction of the *LRC* model (cf. Section 2.3).

5.1 The characteristics of the microstrip

We have characterized resonators with a characteristic impedance of $50\,\Omega$ and $70\,\Omega$. For each resonator we have measured three resonant peaks. Now we compare the results for all peaks quantitatively. In this way we check the consistency of our discussion.

5.1.1 The resonant frequency

We have investigated the influence of the gap width on the positions of the resonant peaks. Our results are shown Fig. 5.1 We see the same behavior for all three resonant peaks. Also there is no difference between the response of the microstrips with characteristic impedances of $50\,\Omega$ and $70\,\Omega$. We observe a steep rise in the resonant frequency for small gap widths. When the gaps get wider the frequency shift approaches a limiting value for the widest gaps. This value is called the unloaded resonant frequency ω_{n} for the nth peak (compare Subsection 2.3.1). We do not see a complete saturation of the resonant frequencies for our values of the gap width. As a conclusion for the gap width $320\,\mu\mathrm{m}$ we still are not in the undercoupled regime.

Finding an exact value of the unloaded resonant frequency is not an easy task. To accomplish it one has to further increase the gap width (compare Subsection 2.3.2

and Section 3.1). For larger gap widths, however, the signal transmitted through the resonator has such a low power that it disappears below the noise spectrum. This was the case for our measurement of a microstrip resonator with the gap width of 640 μm.

5.1.2   The quality factor

For microstrips with characteristic impedances of 50 Ω and 70 Ω we have measured the response of the quality factor on a change of the gap width. The results are shown in Fig. 5.2. For all peaks we see a similar behavior. The points for the characteristic impedance of 70 Ω scatter, however we can see an increasing trend. A variation of the gap width causes a change in the external quality factor of our circuits (compare Subsection 2.3.2 and Section 3.1).

5.1.3   The insertion loss and the internal quality factor

In Fig. 5.3 we plot the insertion loss depending on the gap width. For larger gap widths we see higher insertion losses. The data for the characteristic impedance 50 Ω and 70 Ω are mutually consistent.

The internal quality factor can be calculated using the measured values of the insertion loss IL. The expression [21]

$$Q_{\mathrm{int}} = \frac{Q_{\mathrm{L}}}{1 - 10^{\frac{-IL}{20}}},\tag{5.1}$$

where Q_{L} is the loaded quality factor describes the relation. The values we obtained are presented in Table 5.1. We calculated a value of about 21500 from the first resonant peak. As we can see Q_{L} is very close to Q_{int}, but still slightly lower. This confirms the statement made in Section 5.1.1, that our resonators are still in the overcoupled regime. Therefore we expect that the internal quality factor of our resonator is larger than $2.2 \cdot 10^4$.

	IL (dB)	Q_{L}	Q_{int}
1$^{\mathrm{st}}$ resonant peak	18.6	19000	21500
2$^{\mathrm{nd}}$ resonant peak	19.5	17600	19700

Table 5.1: Evaluation of the internal quality factor for the microstrip resonator from the insertion loss (IL). Results for the microstrip resonator with the gap width of 320 μm. We see that the calculated internal quality factors are lower for the second resonant peak. The reason is frequency dependent loss as described in Subsection 2.4.1.
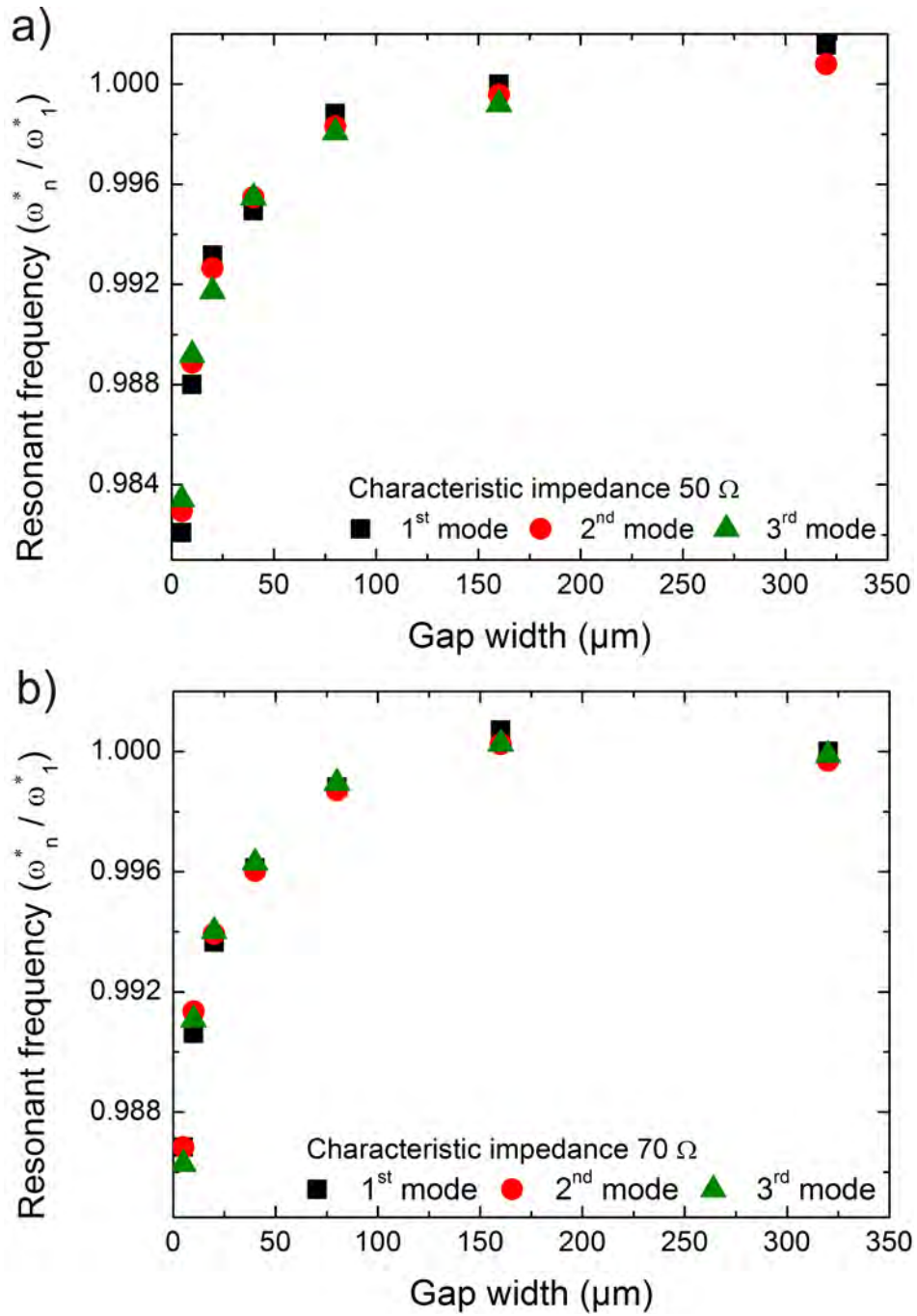
Figure 5.1: Dependence of the resonant frequencies on the gap width. We have normalized to the frequency closest to the unloaded resonant frequency. a) We have normalized to the first resonant frequency of the resonator with the gap width of 160 µm. We have not seen the first resonant peak for the resonator with the gap width of 320 µm. b) We have normalized to the first resonant frequency of the resonator with the gap width of 320 µm.
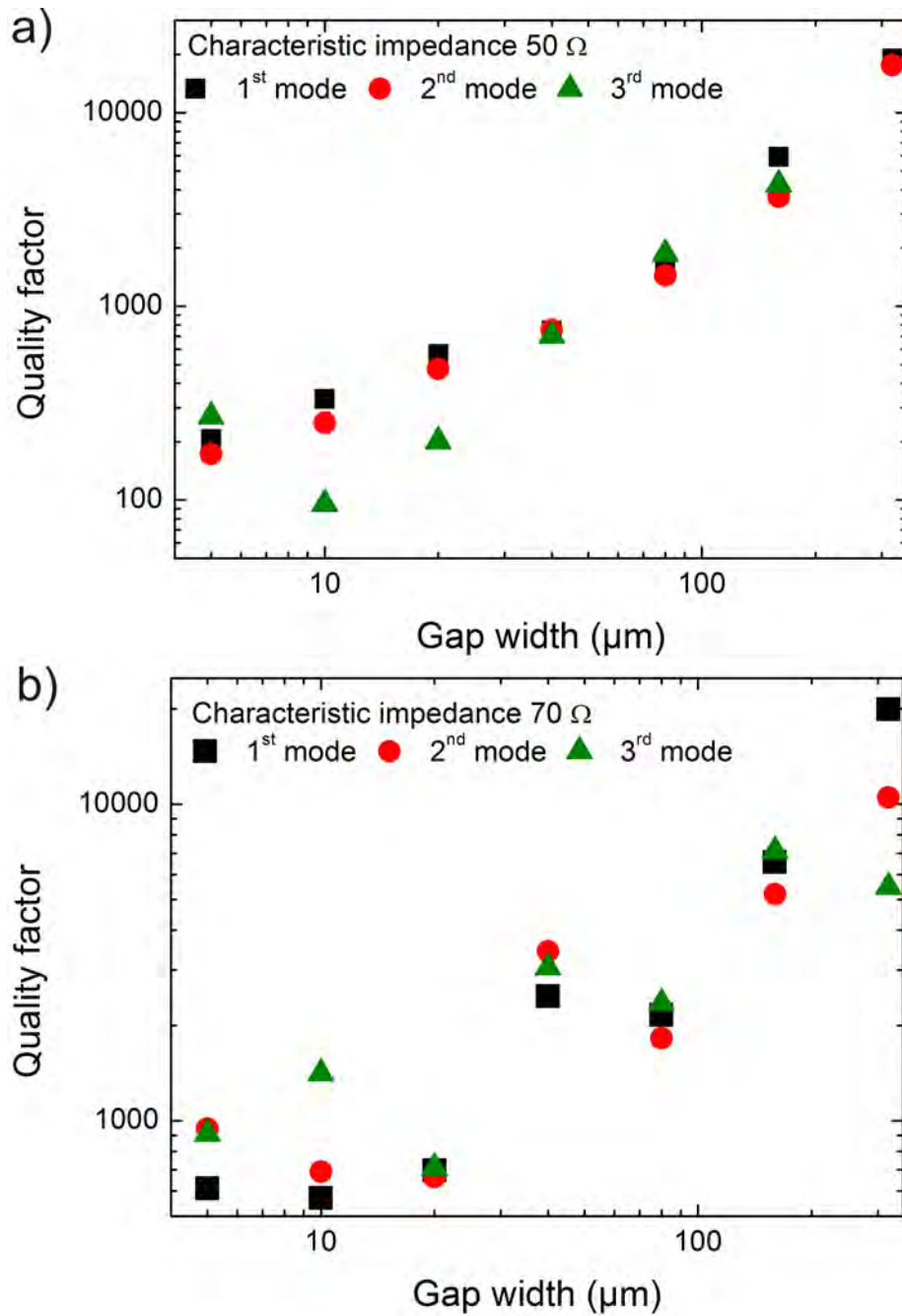
Figure 5.2: Loaded quality factor for microstrips with different gap widths. For larger gap widths the quality factor increases. For the microstrip with the characteristic impedance of $70\,\Omega$ the points scatter. We do not know the reason for this but, we can still observe an increasing tendency.
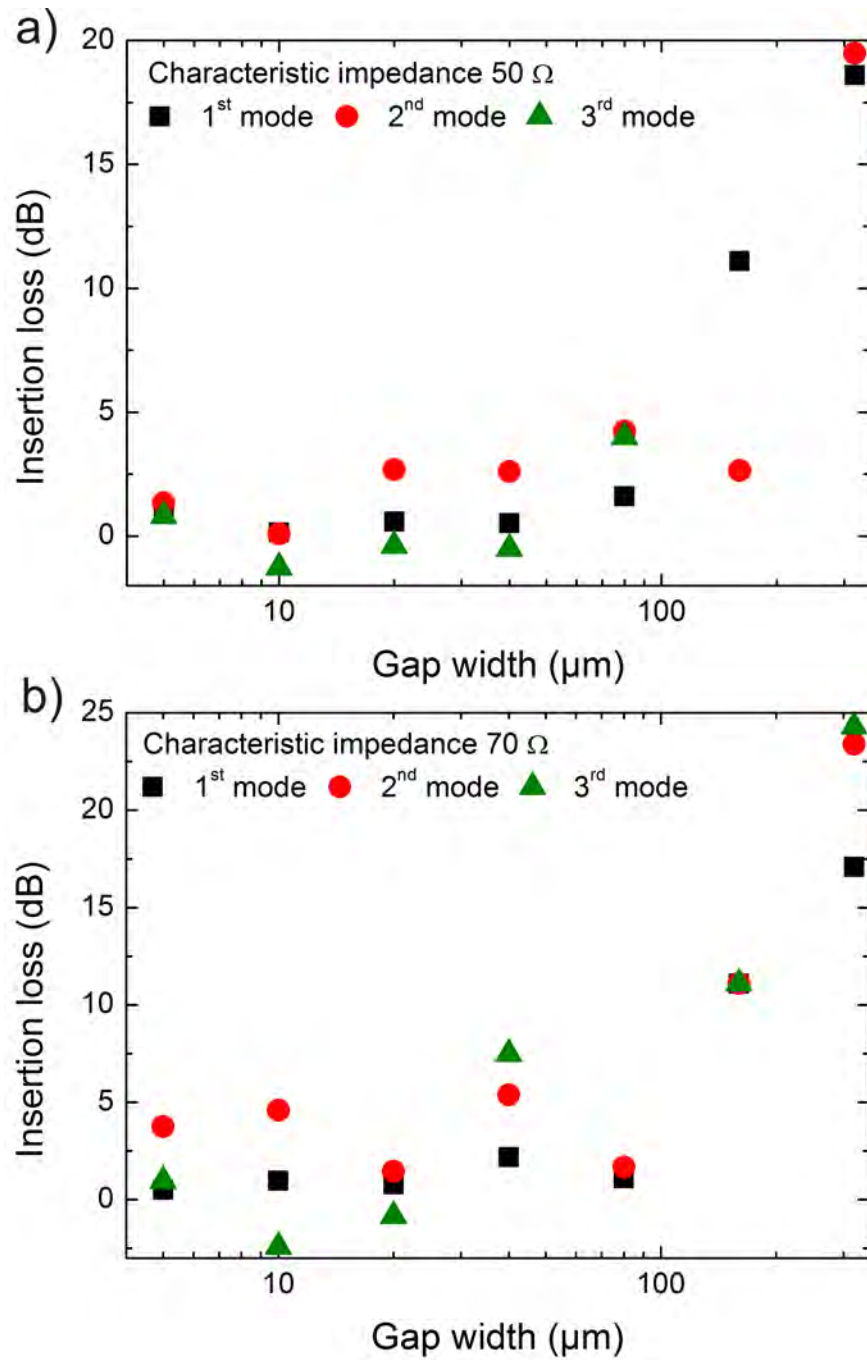
Figure 5.3: The insertion loss for microstrips with different gap widths for the characteristic impedance $50\,\Omega$ and $70\,\Omega$. The points scatter but we see an increasing tendency on both graphs.

5.2　Evaluation of the coupling capacitances

Now we will evaluate the coupling capacitance associated with the gap width of the microstrip resonators. We consider only the resonators with the characteristic impedance of $50\,\Omega$. We apply two methods for this purpose.

Method based on the quality factor and the simulation　The first method is based on the loaded quality factors. By means of the *LRC* model of the microstrip resonator (Section 2.3) we derived a relation between the coupling capacitance C_k^Q and the loaded quality factor Q_L,

$$C_k^Q = \sqrt{\frac{(Q_{\mathrm{int}}/Q_L - 1)\,\frac{\pi n}{2 Z_0 \omega_n}}{2 Q_{\mathrm{int}} \omega R_L + (1 - Q_{\mathrm{int}}/Q_L)\,R_L \frac{\pi n \omega_n}{2}}}. \tag{5.1}$$

For our microstrip circuits the load resistance $R_L = 50\,\Omega$ is equal to the characteristic impedance of the line Z_0. We have already discussed in Section 5.1.1 and Section 5.1.3 that we were not able to extract the values of the internal quality factor Q_{int} and the unloaded resonant frequency ω_n from the measurements. Therefore we have used the following procedure.

Step 1　We initially set the quality factor Q_{int} to be infinite. The frequency ω_n is the frequency of the resonator with the largest gap. For the third resonant peak we have calculated it with Equation 2.4, since we miss the measured value (compare Fig. 5.1).

Step 2　We performed simulations as presented in Section 3.4 and compard the simulated values of the coupling capacitance C_k^{sim} with the measured ones C_k^Q. The effective permittivity in the simulation was adjusted manually so that $C_k^{\mathrm{sim}} = C_k^Q$ holds (lowest standard deviation). Only the values for the first five smallest gap widths were considered[1]. We obtained the effective dielectric constant $\varepsilon_{\mathrm{eff}}$ for the first, second and third peak of 5.5, 4.5 and 4.9, respectively. The resulting value of the permittivity constant is between 1 and 11.9 as predicted by theory (cf. Subsection 2.2). An interesting fact is that the value of $\varepsilon_{\mathrm{eff}}$ varies for different resonant peaks. This is due to frequency-dependent loss mechanisms in the microstrip (compare Subsection 2.4.1).

Step 3　We vary the quality factor Q_{int} to adjust the measurement data C_k^Q to the simulated ones C_k^{sim}. The manual adjustment with the internal quality factor of

---

[1]For low gap widths $Q_L \ll Q_{\mathrm{int}}$ holds. In this regime Equation (5.1) is nearly independent of the choice of the quality factor Q_{int}.

$1 \cdot 10^6$ gave a good agreement. However, values larger than $1 \cdot 10^6$ are not physically meaningful. The results are plotted in Fig. 5.1.

Method based on the resonant frequency The second method we used to obtain the coupling capacitance was based on the measured resonant frequencies ω_n^*. We have evaluated the dependence

$$C_k^f = \frac{1 - \sqrt{1 - \frac{\pi^2 n^2}{4} \left(\frac{\omega_n}{\omega_n^*}\right)^4 \left(\frac{R_L}{Z_0}\right)^2 \left(1 - \frac{\omega_n^{*2}}{\omega_n^2}\right)^2}}{\frac{n\pi\omega_n^3 R_L^2}{2\omega_n^{*2} Z_0} \left(1 - \frac{\omega_n^{*2}}{\omega_n^2}\right)} \tag{5.2}$$

by means of the *LRC* model again. We set the unloaded resonant frequency ω_n so, that the order of magnitude the results based on the resonant frequency C_k^f are mutually consistent with the previous results C_k^f and C_k^{sim}. We obtained the first unloaded resonant frequency as $5.65 \, \text{GHz}$.

In Fig. 5.1 we compare the results for all applied methods. We see that all calculated values show the similar dependence on the gap width. The order of magnitude of the coupling capacitance is $35 \, \text{fF}$ for the gap width of $5 \, \mu\text{m}$ and $4 \, \text{fF}$ for the gap width of $320 \, \mu\text{m}$.

5.3 Description of the microstrip resonators within the LRC model

In the theoretical part we have introduced the *LRC* model to describe the behavior of our resonant circuits in the vicinity of the resonant frequency (cf. Subsection 2.3.1). We now check, whether this model can be appliedto our microstrips with the characteristic impedance $50 \, \Omega$.

We have evaluated expressions describing the characteristics of our resonator as functions of coupling capacitance. For the calculation of the theoretical values we use the simulated coupling capacitance C_k^{sim}.

5.3.1 Frequency dependence on the coupling capacitance

The expression for the measured resonant frequency ω_n^* is

$$\omega_n^* = \frac{1}{\sqrt{\frac{1}{\omega_n^2} + \frac{4Z_0 C_k^{sim}}{n\pi\omega_n \left(1 + \omega_n^2 \left(C_k^{sim}\right)^2 R_L^2\right)}}}. \tag{5.1}$$
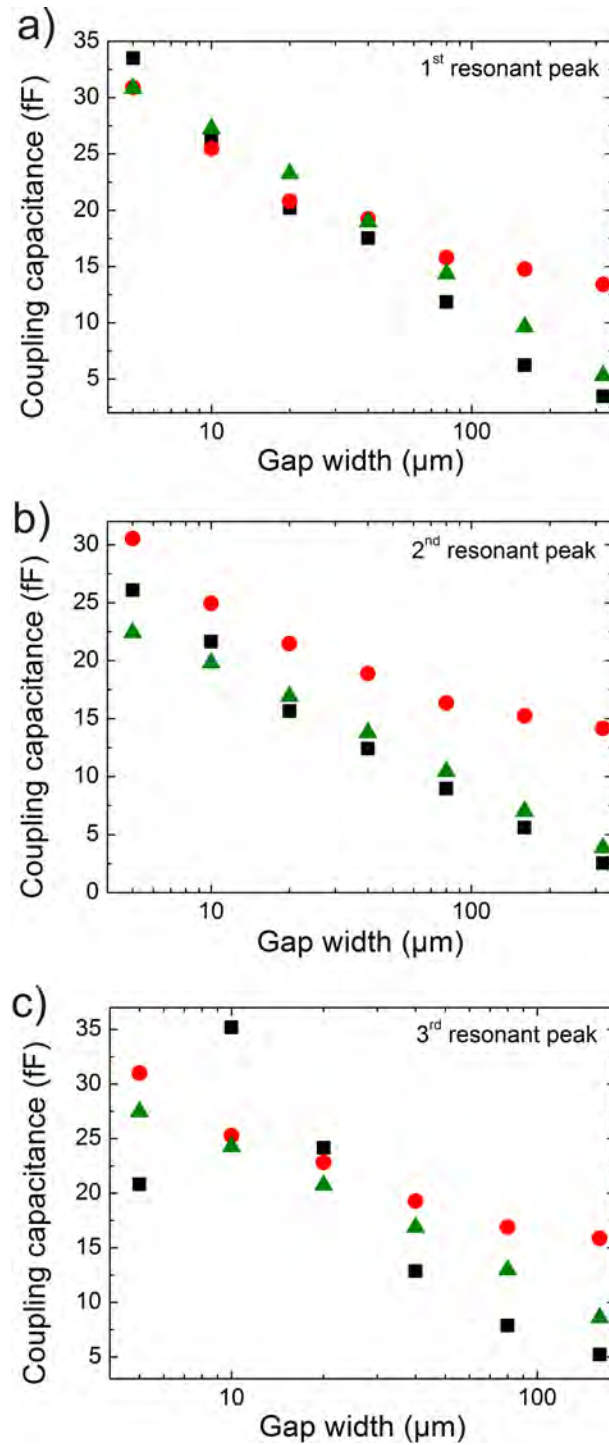
Figure 5.1: Evaluated coupling capacitances for the microstrip resonators with the characteristic impedance $50\,\Omega$. We see that the coupling capacitance decreases for larger gap widths. The coupling capacitance calculated from the quality factor (black rectangles) in agreement with the simulated one (green triangles). The coupling capacitance calculated from the resonant frequency (red circles) is too large for higher gap widths.

In Fig. 5.1 we present the theoretically calculated values of the resonant frequency in comparison with the measured ones. First the order of magnitude of the measured data and the calculated ones is in agreement. For large coupling capacitance the theory describes the slope of the experimental data very well. For small coupling capacitance there is a deviation of 1 % and the slope of the theoretical curve is too steep. This effect can be related to the results presented in Fig. 5.1. There we see that the value of the simulated coupling capacitance C_k^{sim} are higher the values of the coupling capacitance calculated from the resonant frequency C_k^{f}.

5.3.2 Insertion loss dependence on the coupling capacitance

The insertion loss IL of the resonator also depends on the coupling capacitance. The theoretical expression is:

$$IL_{\mathrm{n}} = -20 \log \left(\frac{1}{1 + \frac{\pi n}{4 Z_0 \omega_{\mathrm{n}}^2 \left(C_k^{\mathrm{sim}}\right)^2 R_{\mathrm{L}} Q_{\mathrm{int}}} \left(1 + \omega_{\mathrm{n}}^2 \left(C_k^{\mathrm{sim}}\right) R_{\mathrm{L}}^2\right)} \right). \tag{5.2}$$

As presented in Fig. 5.2 the theory fits well to the data for larger coupling capacitances. However in the undercoupled regime the deviation is 70 %. Again we explain this with the simulated values of the coupling capacitance which are apparently not precise enough in this region.

5.3.3 Quality factor dependence on the coupling capacitance

We have discussed in Section 5.1.3 that all our resonators are still in the overcoupled region. In accordance with the theoretical part (cf. Subsection 2.4.2) the loaded quality factor is then dominated by the external quality factor Q_{ext}

$$Q_{\mathrm{ext}} = \frac{\pi n \left(1 + \omega_{\mathrm{n}}^2 \left(C_k^{\mathrm{sim}}\right) R_{\mathrm{L}}^2\right)}{4 Z_0 \omega_{\mathrm{n}}^2 \left(C_k^{\mathrm{sim}}\right) R_{\mathrm{L}}}. \tag{5.3}$$

In Fig. 5.3 we have plotted the theoretical values of the quality factor Q_{ext} in comparison with the measured data. We see that the theoretical curve fits to the data for the first two resonant peaks for higher values of the coupling capacitances well.

Let us consider the third resonant peak. The theoretical curve lies below the measured data. We can explain this fact by the unprecise choice of the unloaded resonant frequency ω_{n}, since we were not able to determine this value (compare Section. 5.1.1). In addition two data points with the coupling capacitance of 20.7 fF and 24.3 fF are lower then the other values. We do not know the reason for this fact, but it is is agreement with the data presented in Fig. 4.4.
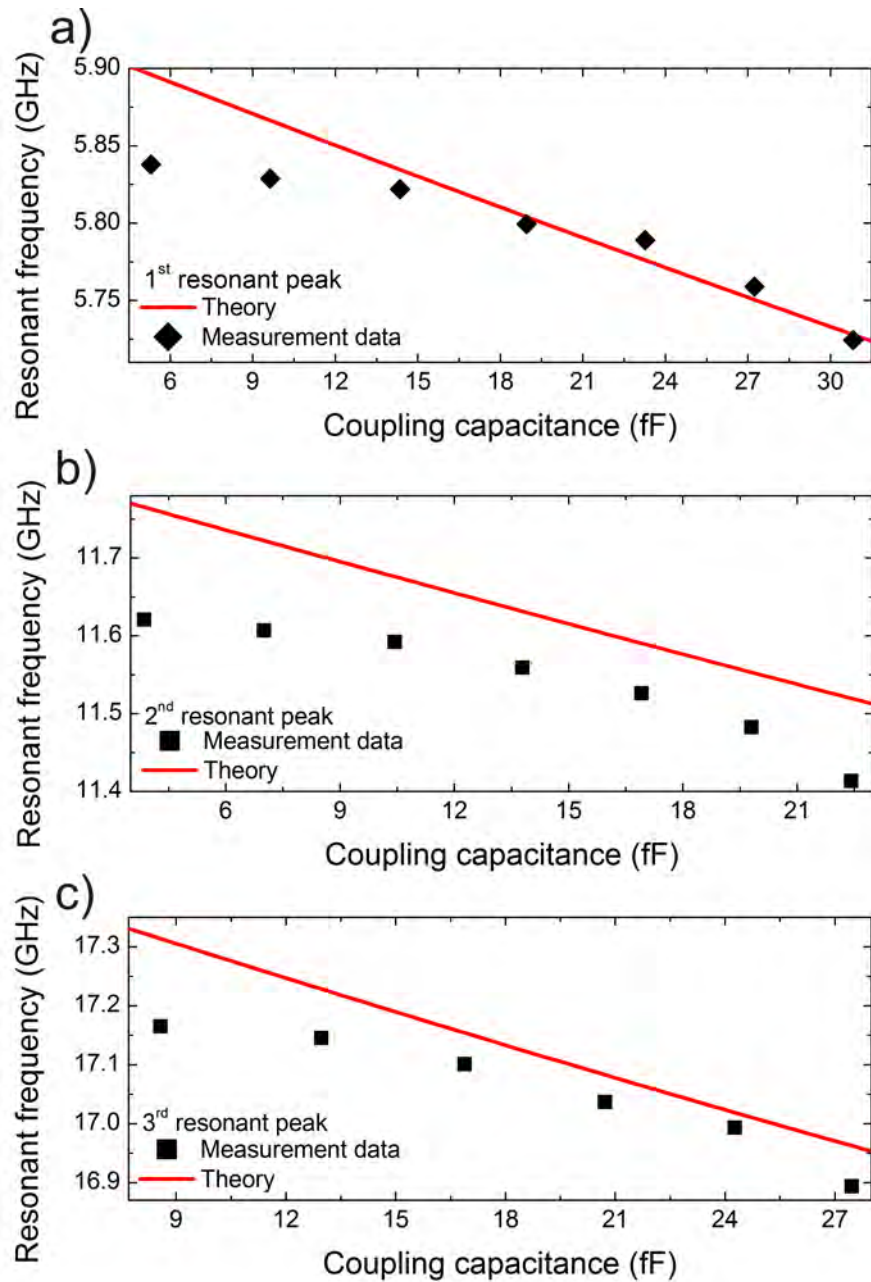
Figure 5.1: In these graphs we plot measured values of the resonant frequency and the theoretical prediction according to the Equation (5.1) against the simulated values of the coupling capacitance. The theory calculates the order of magnitude of the resonant frequency well. Secondly the slope of the theoretical curve describes the behavior of the overcoupled resonators well. For low coupling capacitance we see a deviation of the slope of the theory curve from the measured data.
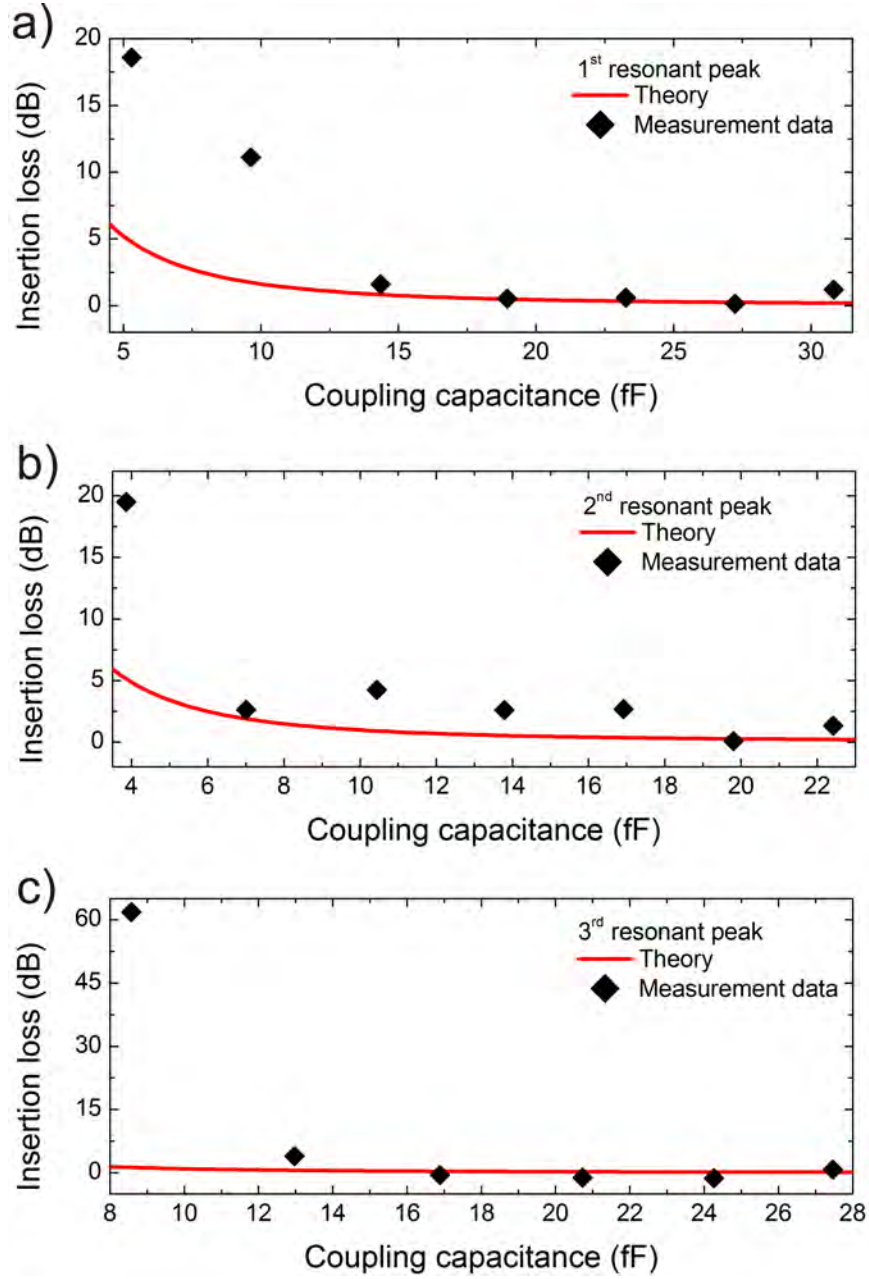
Figure 5.2: Measured values of the insertion loss and theoretical prediction according to Equation (5.2). For higher capacitance values the measured data points lie on the theoretical curve (variation of 1%). However for the low coupling capacitance the measured insertion loss are larger than the theoretical prediction.
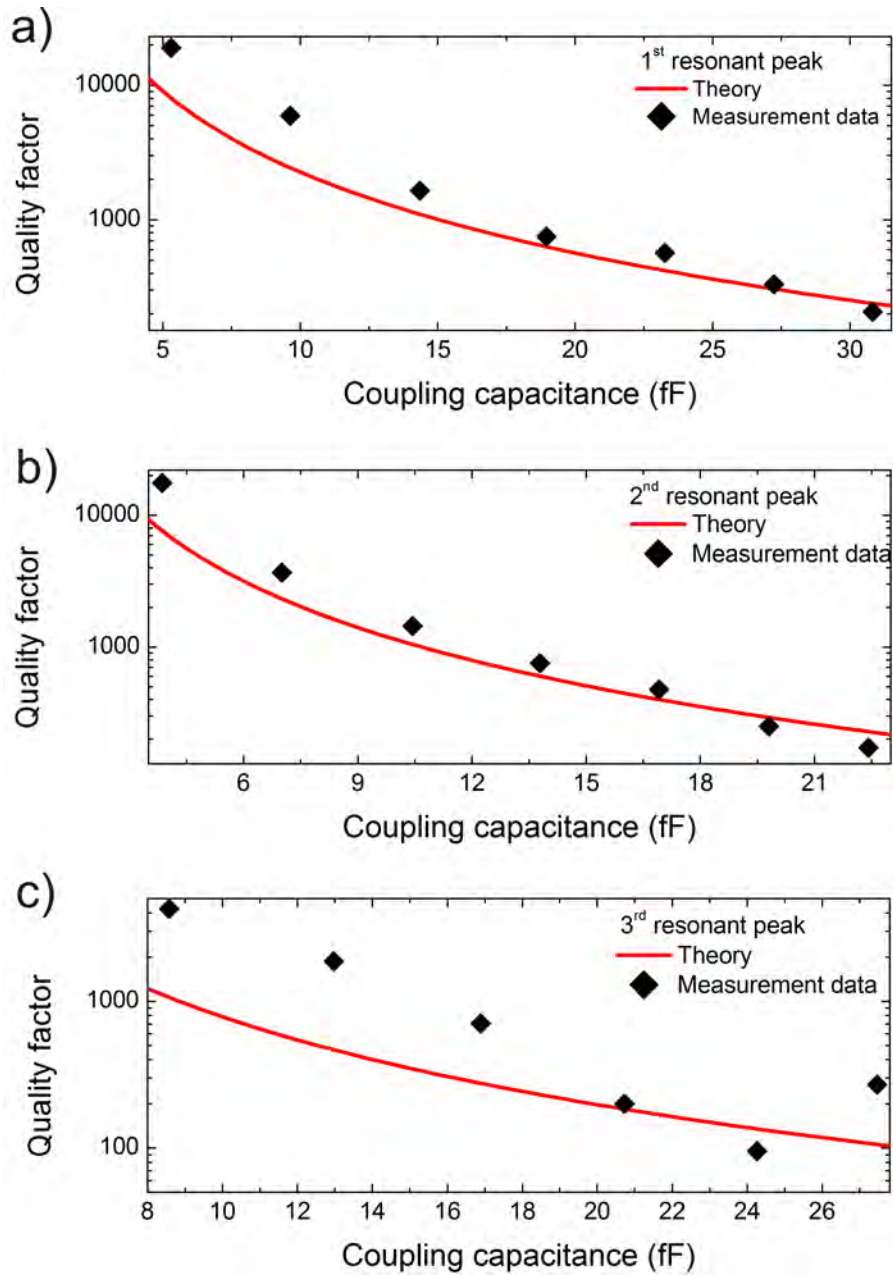
Figure 5.3: Measured values of the loaded quality factor and theoretical prediction according to Equation 5.3. For the first and second resonant peak the theory fits to the measurement data of microstrips well. For the third peak the points scatter are are not in agreement with the theory curve. In our opinion this is due to a calibration problem.

Chapter 6

Summary and Outlook

Circuit QED is a field of physics studying the fundamental interaction between light and matter. During the last years tremendous advancements have been made in improving and extending the functionality of circuit QED systems [12, 60–62]. A new promising superconducting circuit, the microstrip resonator, was studied in this thesis.

We have examined the transmission properties of microstrip resonators with the main focus on the quality factors. The possibilities to tune the quality factors of our resonators were explored. Additionally, we have studied the design parameters necessary to control the resonant frequency of the circuits. For a final verification of applicability of microstrip resonators in circuit QED we have investigated whether constrictions and antennas deteriorate the performance of the resonators.

In the measured frequency spectrum of the microstrip resonant circuits we have observed resonant peaks at about $40\,\mathrm{dB}$ above the background spectrum. No parasitic modes were detected in the examined frequency range. We have tuned the loaded quality factors of our circuits to more than $2 \cdot 10^4$, which is already acceptable for many circuit QED experiments [63]. This order of magnitude was achieved by engineering the coupling capacitance of the circuit.

We have shown that the design and production process used at the WMI allows for full control over the resonant frequency of the studied resonators. We have also demonstrated that the introduction of constrictions does not suppress the resonances in our circuits, quality factors of the resonators even have increased as the constrictions got narrower. In addition we have shown that, depending on the antenna configuration, the quality factors vary from approximately 400 to 1750. As a result, antennas do disturb the performance of the circuits significantly, but through appropriate design we can diminish the unwanted effect.

In addition, we have successfully simulated the coupling capacitance of our circuits. All observed quality factors and resonant frequencies are well understood within the
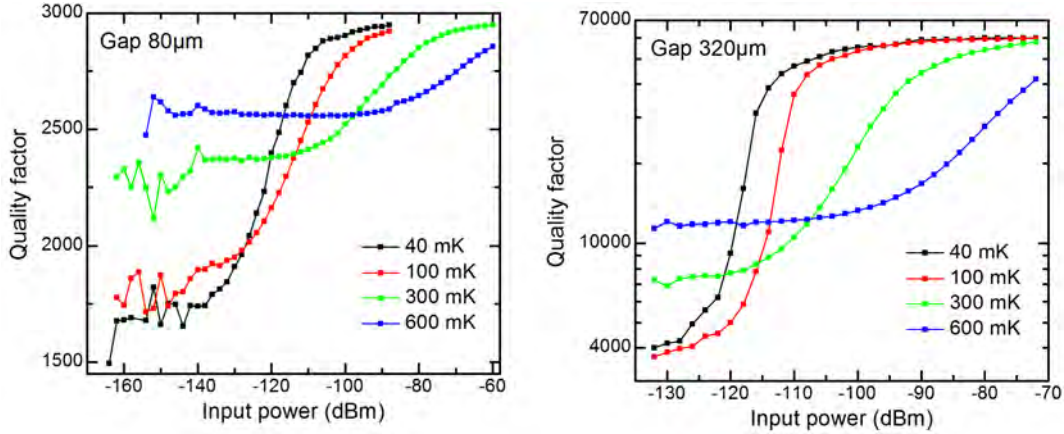
Figure 6.1: Loaded quality factors at milikelvin temperatures as a function of the power applied to the input port of the respective resonator sample. The figure was adopted from Ref. [64]

LRC model.

All in all, we revealed the properties of microstrip resonant circuits making them a very interesting alternative to CPW resonators for applications in circuit QED. The next step is the characterization of microstrip resonators at milikelvin temperatures. Before this thesis was submitted, the measurements of the power and temperature dependence of the quality factors of the resonators fabricated within this work, were already in progress. In the following we report on the first findings for the microstrip resonators with gap widths of $80\,\mu m$ and $320\,\mu m$.

In Fig. 6.1 we show the results recorded at different temperatures ranging from $40 - 600\,mK$ using attenuated input lines and an amplification chain [64]. The values of the probe powers applied correspond to those typically used in circuit QED experiments. We see that the quality factor of the samples saturates at low and high input powers. This phenomenon occurs in the whole temperature range and can be explained with the Two Level Systems in the dielectric. The internal quality factors of the resonators are approximately $4 \cdot 10^3$ which confirms that the microstrip resonators can be successfully applied for experiments in circuit QED. In order to further increase the quality factors we suggest to use another substrate. We propose Sapphire or high-resistivity Silicon [65] possibly without the SiO_2 layer.

Appendix A

Wafer specifications

Manufacturer	CrysTec
Lateral dimensions	$10\,\text{mm} \times 6\,\text{mm}$
Orientation:	100
Thickness:	250 µm
Dopant	Boron (p-type)
Oxide	50nm (thermally oxidized)

Appendix B

Microstrip fabrication parameters

Process step	Details
Wafer cleaning	Ultrasonic bath. Acetone: $2\,\mathrm{min}$, Level 6; Acetone: $2\,\mathrm{min}$, Level 6; Isopropanol: $2\,\mathrm{min}$, Level 6
Niobium sputtering	Pressure: $2.7\,\mathrm{e}-3\,\mathrm{mbar}$; power: $200\,\mathrm{W}$; gas: Argon; gas flow: $10\,\mathrm{sccm/min}$
Wafer cleaning	Ultrasonic bath. Acetone: $2\,\mathrm{min}$, Level 6; Acetone: $2\,\mathrm{min}$, Level 6; Isopropanol: $2\,\mathrm{min}$, Level 6
Resist spinning	AZ 5214 resist, Program 1
Soft bake	Time: $1:10\,\mathrm{min}$; temperature: $110\,\mathrm{°C}$
Edge wall removal	UV radiation intensity: $109\,\mathrm{mJ/cm}^2$
Development	AZ 726 MIF, time: $30\,\mathrm{sec}$,
Mask exposure	UV radiation intensity: $36\,\mathrm{mJ/cm}^2$
Development	AZ 726 MIF, time: $70\,\mathrm{sec}$
RIE physical etching	Time: $90\,\mathrm{sec}$
RIE O_2 plasma ashing	Time: $180\,\mathrm{sec}$
Hot acetone bath	Time: $90\,\mathrm{min}$

Appendix C

Parameters of the samples

The following table contains an overview on some of the designed microstrip resonators and transmission lines. The optical mask refers to the mask labeling system at the WMI. The terms "Basic", "Constriction", "Antenna" and "Mittred bends" refer to the different applied geometries of the samples. The parameter C is the constriction width. Antenna position A is specified relative to the total length of the resonator. "E" refers to a structure with an interrupted conductor line suited for further prcessing with the E-Beam Lithography. "N" refers to the antenna with the narrow end. "N.f." refers to a structure without feed lines. The abbreviations" Prod." and "Char." mean "Produced" and "Characterized" respectively.

Optical mask	Structure	Z_0 (Ω)	g (µm)	C (µm)	A	Prod.	Charact.
Marta 11/05	Basic	50	5	-	-	yes	yes
Marta 11/05	Basic	50	10	-	-	yes	yes
Marta 11/05	Basic	50	20	-	-	yes	yes
Marta 11/05	Basic	50	40	-	-	yes	yes
Marta 11/05	Basic	50	80	-	-	yes	yes
Marta 11/05	Basic	50	160	-	-	yes	yes
Marta 11/05	Basic	50	320	-	-	yes	yes
Marta 11/05	Basic	50	640	-	-	yes	yes
Marta 11/05	Basic	50	N.f.	-	-	yes	yes
Marta 11/05	Basic	70	5	-	-	yes	yes
Marta 11/05	Basic	70	10	-	-	yes	yes
Marta 11/05	Basic	70	20	-	-	yes	yes
Marta 11/05	Basic	70	40	-	-	yes	yes
Marta 11/05	Basic	70	80	-	-	yes	yes

Optical mask	Structure	Z_0 (Ω)	g (µm)	C (µm)	A	Prod.	Charact.
Marta 11/05	Basic	70	160	-	-	yes	yes
Marta 11/05	Basic	70	320	-	-	yes	yes
Marta 11/05	Basic	70	640	-	-	yes	-
Marta 11/05	Basic	70	N.f.	-	-	yes	yes
Marta 11/05	Basic	25	20	-	-	yes	yes
Marta 11/05	Basic	45	20	-	-	yes	yes
Marta 11/05	Basic	60	20	-	-	yes	yes
Marta 11/05	Basic	100	20	-	-	yes	yes
Marta 11/05	Basic	50	-	-	-	-	-
Marta 11/05	Basic	70	-	-	-	-	-
Hoffmann_2011	Constriction	50	80	1	-	-	-
Hoffmann_2011	Constriction	50	80	1 (E)	-	-	-
Hoffmann_2011	Constriction	50	80	2	-	yes	yes
Hoffmann_2011	Constriction	50	80	5	-	yes	yes
Hoffmann_2011	Constriction	50	80	10	-	yes	yes
Hoffmann_2011	Constriction	50	80	25	-	yes	yes
Hoffmann_2011	Constriction	50	80	50	-	yes	yes
Hoffmann_2011	Constriction	50	80	100	-	yes	yes
Hoffmann_2011	Constriction	70	80	2	-	yes	yes
Hoffmann_2011	Constriction	50	320	1	-	-	-
Hoffmann_2011	Constriction	50	320	1 (E)	-	-	-
Hoffmann_2011	Constriction	50	320	2	-	yes	yes
Hoffmann_2011	Constriction	50	320	5	-	yes	yes
Hoffmann_2011	Constriction	50	320	10	-	yes	yes
Hoffmann_2011	Constriction	50	320	25	-	yes	yes
Hoffmann_2011	Constriction	50	320	50	-	yes	yes
Hoffmann_2011	Constriction	50	320	100	-	yes	yes
Hoffmann_2011	Constriction	70	320	2	-	-	-
Hoffmann_2011	Antenna	50	80	-	0.5	yes	yes
Hoffmann_2011	Antenna	50	80	-	0.5 (N)	yes	yes
Hoffmann_2011	Antenna	50	80	-	0.25	yes	yes

Optical mask	Structure	Z_0 (Ω)	g (μm)	C (μm)	A	Prod.	Charact.
Hoffmann_2011	Antenna	50	80	-	0.5; 0.5	yes	yes
Hoffmann_2011	Antenna	50	80	-	0.25; 0.75	yes	yes
Hoffmann_2011	Basic	172	80	-	-	-	-
Hoffmann_2011	Basic	156	80	-	-	-	-
Hoffmann_2011	Basic	136	80	-	-	-	-
Hoffmann_2011	Basic	120	80	-	-	-	-
Hoffmann_2011	Mitred bends	50	80	-	-	-	-
Wulschner_2011	Basic	50	300	-	-	-	-
Wulschner_2011	Basic	50	340	-	-	-	-
Wulschner_2011	Constriction	50	80	-	-	-	-
Wulschner_2011	Constriction	50	320	-	-	-	-
Wulschner_2011	Antenna	50	80	-	-	-	-

List of Figures

List of Tables

Bibliography

[1] A. Einstein, Concerning an Heuristic Point of View Toward the Emission and Transformation of Light, *Ann. Phys.* 17, 132 (1905).

[2] J. M. Raimond, M. Brune, and S. Haroche, Manipulating quantum entanglement with atoms and photons in a cavity, *Rev. Mod. Phys.* 73, 565 (2001).

[3] H. Mabuchi and A. C. Doherty, Cavity Quantum Electrodynamics: Coherence in Context, *Science* 298, 1372 (2002).

[4] H. Walther, B. T. H. Varcoe, B.-G. Englert, and T. Becker, Cavity quantum electrodynamics, *Rep. Prog. Phys.* 69, 1325 (2006).

[5] A. Wallraff, D. I. Schuster, A. Blais, L. Frunzio, R.-S. Huang, J. Majer, S. Kumar, S. M. Girvin, and R. J. Schoelkopf, Strong coupling of a single photon to a superconducting qubit using circuit quantum electrodynamics, *Nature* 431, 162 (2004).

[6] R. J. Schoelkopf and S. M. Girvin, Wiring up quantum systems, *Nature* 451, 664 (2008).

[7] F. Deppe, M. Mariantoni, E. P. Menzel, A. Marx, S. Saito, K. Kakuyanagi, H. Tanaka, T. Meno, K. Semba, H. Takayanagi, E. Solano, and R. Gross, Two photon probe of the Jaynes-Cummings model and controlled symmetry breaking in circuit QED, *Nature Physics* 4, 686 (2008).

[8] I. I. Rabi, Space Quantization in a Gyrating Magnetic Field, *Phys. Rev.* 51, 652 (1937).

[9] I. Chiorescu, Y. Nakamura, C. J. P. M. Harmans, and J. E. Mooij, Coherent Quantum Dynamics of a Superconducting Flux Qubit, *Science* 299, 1869 (2003).

[10] R. P. Feynman, Simulating Physics with Computers, *Int. J. Theor. Phys.* 21, 465 (1982).

[11] M. Mariantoni, H. Wang, T. Yamamoto, M. Neeley, R. C. Bialczak, Y. Chen, M. Lenander, E. Lucero, A. D. OConnell, D. Sank, M. Weides, J. Wenner, Y. Yin, J. Zhao, A. N. Korotkov, A. N. Cleland, and J. M. Martinis, Implementing the Quantum von Neumann Architecture with Superconducting Circuits, *Science* 334, 61 (2011).

[12] T. Niemczyk, F. Deppe, H. Huebl, E. P. Menzel, F. Hocke, M. J. Schwarz, J. J. Garcia-Ripoll, D. Zueco, T. Hümmer, E. Solano, A. Marx, and R. Gross, Circuit quantum electrodynamics in the ultrastrong-coupling regime, *Nature Physics* 6, 772 (2010).

[13] M. Göppl, A. Fragner, M. Baur, R. Bianchetti, S. Filipp, J. M. Fink, P. J. Leek, G. Puebla, L. Steffen, and A. Wallraff, Coplanar Waveguide Resonators for Circuit Quantum Electrodynamics, *J. Appl. Phys.* 104, 113904 (2008).

[14] G. Benz, T. A. Scherer, M. Neuhaus, and W. Jutzi, Quality Factor and Intermodulation Product of Superconducting Coplanar Wave Guides with Slots in a DC Magnetic Field, *IEEE Trans. Appl. Supercond.* 9, 3046 (1999).

[15] X. Wu, I. Awai, Z. Yan, K. Wada, and T. Moriyoshi, Quality factors of coplanar waveguide resonators, in *Microwave Conference, 1999 Asia Pacific*, vol. 3, 670 −673 vol.3 (1999).

[16] T. Itoh and R. Mittra, Analysis of a microstrip disk resonator, *Arch. Elek. Übertragung* 27, 456 (1973).

[17] J. Wollf and N. Knoppik, Rectangular and circular micorstrip disc capacitors and resonators, in *The European Micorwave Conf. Brussels, Belgium* (1973).

[18] T. Itoh, Analysis of Microstrip Resonators, *IEEE Trans. Microw. Theory Tech.* 22, 946 (1974).

[19] R. E. Collin, *Foundations for Microwave Engineering*, The Institute of Electrical and Electronics Engineers, Inc., 2nd edn. (2001).

[20] A. D. OConnell, M. Ansmann, R. C. Bialczak, M. Hofheinz, N. Katz, E. Lucero, C. McKenney, M. Neeley, H. Wang, E. M. Weig, A. N. Cleland, and J. M. Martinis, Microwave dielectric loss at single photon energies and millikelvin temperatures, *Appl. Phys. Lett.* 92, 112903 (2008).

[21] J. M. Sage, V. Bolkhovsky, W. D. Oliver, B. Turek, and P. B. Welander, Study of loss in superconducting coplanar waveguide resonators, *J. Appl. Phys.* 109, 23 (2011).

[22] G. Ghione and C. U. Naldi, Coplanar Waveguides for MMIC Applications: Effect of Upper Shielding, Conductor Backing, Finite-Extent Ground Planes, and Line-to-Line Coupling, *IEEE Trans. Microw. Theory Tech.* 35, 260 (1987).

[23] T. Weissl, *Two-Resonator Circuit-QED: Two Coupled Resonators on a Chip*, Diploma thesis, Technische Universität München (2006).

[24] D. M. Pozar, *Microwave Engineering*, Wiley and Sons Ltd., 3rd edn. (2009).

[25] J. S. Beasley and G. M. Miller, *Modern Electronic Communication*, Prentice Hall (2007).

[26] H. H. Meinke and F. W. Gundlach, *Taschenbuch Der Hochfrequenztechnik: Band 2: Komponenten*, Springer-Verlag (1992).

[27] T. P. Orlando and K. A. Delin, *Fundations of Applied Superconductivity*, Adison-Wesley Publishing Company (1990).

[28] W. J. Wallace and R. H. Silsbee, Microstrip resonators for electronspin resonance, *Rev. Sci. Instrum.* 62, 1754 (1991).

[29] T. Niemczyk, *From strong to ultrastrong coupling in circuit QED architecturess*, Ph.D. thesis, Technische Universität München (2011).

[30] K. Küpfmüller, W. Mathis, and A. Reibiger, *Theoretische Elektrotechnik*, Springer Berlin, Heidelberg (2006).

[31] D. I. Schuster, *Circuit Quantum Electrodynamics*, Ph.D. thesis, Yale University (2007).

[32] L. N. Cooper, Bound electron pairs in a degenerate Fermi gas, *Phys. Rev.* 104, 1189 (1956).

[33] M.Peiniger and H.Piel, A Superconducting Nb3Sn Coated Multicell Accelerating Cavity, *IEEE Trans. Nucl. Sci.* 32, 3610 (1985).

[34] B. Aune, R. Bandelmann, D. Bloess, B. Bonin, A. Bosotti, M. Champion, C. Crawford, G. Deppe, B. Dwersteg, D. A. Edwards, H. T. Edwards, M. Ferrario, M. Fouaidy, P.-D. Gall, A. Gamp, A. Gössel, J. Graber, D. Hubert, M. Hüning, M. Juillard, T. Junquera, H. Kaiser, G. Kreps, M. Kuchnir, R. Lange, M. Leenen, M. Liepe, L. Lilje, A. Matheisen, W.-D. Möller, A. Mosnier, H. Padamsee, C. Pagani, M. Pekeler, H.-B. Peters, O. Peters, D. Proch, K. Rehlich, D. Reschke, H. Safa, T. Schilcher, P. Schmüser, J. Sekutowicz, S. Simrock, W. Singer,

M. Tigner, D. Trines, K. Twarowski, G. Weichert, J. Weisend, J. Wojtkiewicz, S. Wolff, and K. Zapfe, Superconducting TESLA cavities, *Phys. Rev. ST Accel. Beams* 3, 092001 (2000).

[35] D. P. Pappas, M. R. Vissers, D. S. Wisbey, J. S. Kline, and J. Gao, Two Level System Loss in Superconducting Microwave Resonators, *IEEE Trans. Appl. Supercond.* 21, 871 (2011).

[36] J. M. Martinis, K. B. Cooper, R. McDermott, M. Steffen, M. Ansmann, K. D. Osborn, K. Cicak, S. Oh, D. P. Pappas, R. Simmonds, and C. C. Yu, Decoherence in Josephson Qubits from Dielectric Loss, *Phys. Rev. Lett.* 95, 210503 (2005).

[37] B. A. Mazin, *Microwave Kinetic Inductance Detectors*, Ph.D. thesis, California Institute of Technology (2004).

[38] M. Hiebel, *Grundlagen der vektoriellen Netzwerkanalyse*, Rohde and Schwarz, 2nd edn. (2007).

[39] M. Häberlein, The desing of the resonant frequency of microstrip resonators. Private communication (2011).

[40] H.-G. Wagemann and T. Schönauer, *Silizium-Planartechnologie: Grundprozesse, Physik und Bauelemente*, Teubner Verlag (2003).

[41] E. P. Menzel, F. Deppe, M. Mariantoni, M. A. A. Caballero, A. Baust, T. Niemczyk, E. Hoffmann, A. Marx, E. Solano, and R. Gross, Dual-path state reconstruction scheme for propagating quantum microwaves and detector noise tomography, *Phys. Rev. Lett.* 105, 100401 (2010).

[42] E. Hoffmann, F. Deppe, T. Niemczyk, T. Wirth, E. P. Menzel, G. Wild, H. Huebl, M. Mariantoni, T. Weißl, A. Lukashenko, A. P. Zhuravel, A. V. Ustinov, A. Marx, and R. Gross, A Superconducting 180° Hybrid Ring Coupler for circuit Quantum Electrodynamics, *Appl. Phys. Lett.* 97, 222508 (2010).

[43] M. Kirschning, R. Jansen, and N. Koster, Measurement and Computer-Aided Modeling of Microstrip Discontinuities by an Improved Resonator Method, in *Microwave Symposium Digest, 1983 IEEE MTT-S International* (1983).

[44] R. C. Jaeger, *"Lithography". Introduction to Microelectronic Fabrication*, Upper Saddle River: Prentice Hall (2002).

[45] L. Frunzio, A. Wallraff, D. Schuster, J. Majer, and R. Schoelkopf, Fabrication and Characterization of SuperconductingCircuit QED Devices for Quantum Computation, *IEEE Trans. Supercond.* 15, 233603 (2005).

[46] M. Madou, *Fundamentals of Microfabrication*, CRC Press, Florida, 6th edn. (2002).

[47] S. M. S. Gary S. May, *Fundamentals of Semiconductor Fabrication*, Wiley and Sons (2003).

[48] R. DeCarlo, *Handbook of organic solvent properties*, Prentice Hall (1989).

[49] I. Smallwood, *Encyclopedia of Statistical Sciences*, Arnold London (1996).

[50] K. Nabors and J. White, FastCap: A Multipole Accelerated 3-D Capacitance Extraction Program, *IEEE Trans. Comput.-Aided Design* 10, 1447 (1991).

[51] S.Kotz, *Linear Systems: A State Variable Approach with Numerical Implementation*, John Wiley and Sons (2006).

[52] H. Wollnik and H. Ewald, The influence of magnetic and electric fringing fields on the trajectories of charged particles, *Nucl. Instrum. Methods* 36, 93 (1965).

[53] *Formelzeichen für die Elektrotechnik Teil 3: Logarithmische und verwandte Größen und ihre Einheiten*, DIN IEC 60027-3:2002 (2002).

[54] *Teledyne Reynolds TRUE BLUE (TM). Cable specifications. http://www.teledynereynolds.co.uk.*

[55] O. Astafiev, K. O. Inomata, A. Niskanen, T. Yamamoto, Y. A. Pashkin, Y. Nakamura, and J. S. Tsai, Single artificial-atom lasing, *Nature* 449, 588 (2007).

[56] P. K. Day, H. G. LeDuc, B. A. Mazin, A. Vayonakis, and J. Zmuidzinas, A broadband superconducting detector suitable for use in large arrays, *Nature* 425, 817 (2003).

[57] K.Yoshida, K.Watanabe, T.Kisu, and K.Enpuku, Evaluation of Magnetic Penetration Depth and Surface Resistance of Superconducting Thin Films using Coplanar Waveguides, *IEEE Trans. Appl. Supercond.* 5, 1979 (1996).

[58] T. H. Lee, *Planar Microwave Engineering: A Practical Guide to Theory, Measurement, and Circuits*, Cambridge University Press (2004).

[59] A. E. Miroshnichenko, S. Flach, and Y. S. Kivshar, Fano resonances in nanoscale structures, *Rev. Mod. Phys.* 82, 2257 (2010).

[60] E. Lucero, M. Hofheinz, M. Ansmann, R. C. Bialczak, N. Katz, M. Neeley, A. D. OConnell, H. Wang, A. N. Cleland, , and J. M. Martinis, High-Fidelity Gates in a Single Josephson Qubit, *Phys. Rev. Lett.* 100, 247001 (2008).

[61] L. DiCarlo, J. M. Chow, J. M. Gambetta, L. S. Bishop, B. R. Johnson, D. I. Schuster, J. Majer, A. Blais, L. Frunzio, S. M. Girvin, and R. J. Schoelkopf, Demonstration of two-qubit algorithms with a superconducting quantum processor, *Nature* 460, 240 (2009).

[62] S. D. Liberato, D. Gerace, I. Carusotto, and C. Ciuti, Extracavity quantum vacuum radiation from a single qubit, *Phys. Rev. A* 80, 053810 (2009).

[63] A. Baust and F. Deppe, Quality factors required for experiments in circuit QED. Personal communication (2011).

[64] A. Baust, M. Krawczyk, M. Häberlein, E. Hoffmann, U. Ehmann, N. Kalb, F. Deppe, A. Marx, and R. Gross, Superconducting Microstrip Resonators for Circuit Quantum Electrodynamics Experiments, in R. Hackl and H. Hübl (editors), *Annual Report*, Walther-Meissner-Institut (2011).

[65] B. Rong, J. N. Burghartz, Fellow, L. K. Nanver, B. Rejaei, and M. van der Zwan, Surface-Passivated High-Resistivity Silicon Substrates for RFICs, *IEEE Electr. Device L.* 25, 176 (2004).

Acknowledgements

On this page I would like to express my appreciation to the people who have supported me during the work on this master thesis.

This thesis could not have been written without Prof. Dr. Rudolf Gross who has allowed me to spend a research year at the Walther-Meißner-Institut. In addition he was always open for all my questions and suggestions. Discussions with him as well as his lectures have been an inspiration for me all the time.

I am very thankful to Dr. Achim Marx for his support during my activities at the WMI. In the course of my work he has given me many useful advices. I also appreciate very much his proposals to enrich this thesis and his interdisciplinary knowledge.

For many valuable discussions and ideas I thank Dr. Frank Deppe. I am very grateful, that he has allowed me to go to the 4th Workshop on the Physics and Applications of Superconducting Microresonators organized by the International Research Institute for Radio Astronomy in Grenoble, France. In front of an international audience I presented the achievements of my colleagues and my own there. It was a very worthwhile experience for me.

I truly thank my advisor Alexander Baust who have encouraged and challenged me in the course of my thesis. He always had time for my questions and suggestions and he has put an enormous effort to support me in my activities. I have learned a lot from him during this year about physical concepts and measurement techniques. I appreciate a lot his attitude, which is aim-oriented and simply makes things go forward. It was a pleasure and delight to work with him.

I would like to thank Peter Eder for the support he gave me during my thesis. I appreciate his lovely attitude and his jokes. His presence was very important to me. He brings a great athmosphere into the group.

I would like to express my gratitude to the wonderful Ph.D. students at the WMI. Elisabeth Hoffmann has showed me the production process and was my mentor during my activity as a working student. I appreciate professional opinions of Edwin Menzel about my results and possible interpretations of them. Max Häberlein gave me numerous valuable suggestions. Ling Zhong have exchanged here experiences about CPW resonators with me. I also thank all other members of the Quantum Information Processing group at the WMI who gave me a lot of support: Thomas Niemczyk (former member), Dr. Hans Hübl, Jan Götz, Karl Friedrich Wulschner, Manuel Schwarz, Fredrik Hocke.

Declaration of Originality

I, Marta Krawczyk hereby certify, that the submitted master thesis is my own work and it does not contain any material previously published or substantially overlap with material submitted for the award of any other degree at any institution. Information derived from the published and unpublished work of others has been acknowledged in the text and a list of references is given in the bibliography.

Signature
Munich, 9th January 2012